Geophysical Journal International

Geophys. J. Int. (2019) **219,** S115–S136
Advance Access publication 2019 May 21
GJI Rock and Mineral Physics, Rheology

doi: 10.1093/gji/ggz231

Lowermost mantle thermal conductivity constrained from experimental data and tomographic models

Frédéric Deschamps[1] and Wen-Pin Hsieh[1,2]

[1] *Institute of Earth Sciences, Academia Sinica,* 128 *Academia Road Sec.* 2, *Nangang, Taipei* 11529, *Taiwan. E-mail: frederic@earth.sinica.edu.tw*
[2] *Department of Geosciences, National Taiwan University, Taipei* 10617, *Taiwan*

Accepted 2019 May 16. Received 2019 May 2; in original form 2018 September 17

SUMMARY

Heat transfer through Earth's mantle is sensitive to mantle thermal conductivity and its variations. Thermal conductivities of lower mantle minerals, bridgmanite (Bm) and ferropericlase (Fp), depend on pressure, temperature, and composition. Because temperature and composition are expected to strongly vary in the deep mantle, thermal conductivity may also vary laterally. Here, we compile self-consistent data on lattice thermal conductivities of Bm and Fp at high pressure to model lower mantle thermal conductivity and map its possible lateral variations. Importantly, our data set allows us to quantify the influence of iron content on mantle conductivity. At the bottom of the mantle, the thermal conductivity for a pyrolitic mantle calculated along an adiabat with potential temperature 2000 K is equal 8.6 W m^{-1} K^{-1}. Using 3-D thermochemical models from probabilistic tomography, which include variations in temperature, iron content, and bridgmanite fraction, we then calculate possible maps of conductivity anomalies at the bottom of the mantle. In regions known as low shear-wave velocity provinces, thermal conductivity is reduced by up to 26 per cent compared to average mantle, which may impact mantle dynamics in these regions. A simple analysis of threshold and saturation effects related to the iron content shows that our estimates of thermal conductivity may be considered as upper bounds. Quantifying these effects more precisely however requires additional mineral physics measurements. Finally, we estimate variations in core–mantle boundary heat flux, and find that that these variations are dominated by lateral temperature anomalies and are only partly affected by changes in thermal conductivity.

Key words: Composition and structure of the mantle; High-pressure behaviour; Heat flow; Mantle processes.

1 INTRODUCTION

Lattice thermal conductivities of mantle minerals typically increase with pressure but decrease with increasing temperature (e.g. Klemens *et al.* 1962). In Earth's mantle temperature regularly increases with depth, such that these two effects are partially balancing each other. Based on ambient condition data and thermodynamic modeling, Hofmeister (1999) calculated radial profiles along mantle adiabat and found that conductivity increases by about a factor 2.5 from top to bottom of Earth's mantle. At a given depth (pressure), temperature is very likely to vary laterally, thus inducing lateral changes in thermal conductivity, which may, in turn, impact mantle dynamics. Such variations could, in particular, stabilize and thicken thermal plumes (Dubuffet & Yuen 2000) and thin downwellings (Dubuffet *et al.* 2000).

Earth's mantle thermal conductivity further depends on mantle's mineralogical composition, that is in the lower mantle, the relative fractions of dominant minerals, bridgmanite [$(Mg,Fe)SiO_3$] and ferropericlase [(Mg,Fe)O], and on the amount of iron within these minerals. At ambient pressure, periclase (MgO) is thermally more conductive than pure magnesium bridgmanite ($MgSiO_3$) by about a factor 5 (Dalton *et al.* 2013; Hsieh *et al.* 2017), a difference that increases with pressure. Recently, several experimental studies have measured the influence of iron on the lattice thermal conductivities of bridgmanite (Hsieh *et al.* 2017) and ferropericlase (Goncharov *et al.* 2015; Ohta *et al.* 2017; Hsieh *et al.* 2018). Interestingly, at lowermost mantle pressure, conductivities of iron and iron-aluminum bearing bridgmanite [Fe-Bm and (Fe,Al)-Bm] are approximately two times smaller than that of pure $MgSiO_3$ (Hsieh *et al.* 2017). The conductivity of ferropericlase (Fp) is

also substantially lower than that of periclase. At 120 GPa and ambient temperature, for instance, the conductivity of ferropericlase with 10 per cent iron is around 50 $W\,m^{-1}\,K^{-1}$ (Hsieh *et al.* 2018), much lower than the extrapolated value for MgO, around 280 $W\,m^{-1}\,K^{-1}$ (Dalton *et al.* 2013).

Lateral variations in temperature and composition thus potentially induce strong variations in mantle thermal conductivity. Lower mantle seismic structure provides key information about the thermochemical variations in these regions. In the lowermost mantle ($z \geq 2400$ km), this structure is dominated by two large low shear-wave velocity provinces (LLSVPs) below Africa and the Pacific, where shear-wave speed is reduced by a few per cent compared to its horizontal average (for a comparison of tomographic models published between 2005 and 2010, see Ritsema *et al.* 2011). The nature of the LLSVPs is still debated. Several observations, however, suggest that they are chemically distinct from the rest of the mantle (e.g. van der Hilst and Kárason 1999; Masters *et al.* 2000; Deschamps & Trampert 2003; Trampert *et al.* 2004). In addition, recent density estimates from solid Earth tide measurments and modelling (Lau *et al.* 2017) indicate that they may be denser than average mantle by ∼0.5 per cent, a conclusion previously reached by normal mode seismology (Ishii & Tromp 1999; Trampert *et al.* 2004; Mosca *et al.* 2012). A likely explanation for density excess and low shear-wave velocity is that LLSVPs are enriched in iron oxide by up to a few per cent compared to average mantle (Trampert *et al.* 2004; Deschamps *et al.* 2012; Mosca *et al.* 2012). LLSVPs are further believed to be hotter than average mantle, typically by up to 400 K (Trampert *et al.* 2004; Mosca *et al.* 2012), the thermal decrease in density being overcompensated by the intrinsic chemical increase due to iron enrichment.

Here, we develop a method to model lower mantle thermal conductivity from a self-consistent mineral physics data set (Dalton *et al.* 2013; Hsieh *et al.* 2017, 2018). We then apply this method to infer possible maps of anomalies in lower mantle thermal conductivity and core–mantle boundary (CMB) heat flux using available thermochemical models of lower mantle (Trampert *et al.* 2004; Mosca *et al.* 2012).

2 EXPERIMENTAL DATA

Our modelling of Earth's lower mantle thermal conductivity is based on a compilation of recent measurements of lattice thermal conductivities of single crystals of bridgmanite (Hsieh *et al.* 2017), periclase (Dalton *et al.* 2013) and ferropericlase (Hsieh *et al.* 2018) at room temperature and high pressure (Fig. 1). Bridgmanite (Bm) data include measurements for pure magnesium bridgmanite, $MgSiO_3$, iron-bearing bridgmanite with fraction of iron, x_{Fe}^{Bm}, equal to 0.072 (Bm7.2) and iron–aluminum-bearing bridgmanite with $x_{Fe}^{Bm} = 0.129$ (Al-Bm12.9). Ferropericlase data include three different samples with fraction of iron, x_{Fe}^{Fp}, of 0.08, 0.10 and 0.56 (Fp8, Fp10 and Fp56), respectively. Except for MgO, measurements have been performed up to pressure of approximately 120 GPa. All measurements were performed at room temperature. The detailed influence of temperature on thermal conductivity is still unclear, but several experiments indicate that iron bearing materials may follow a $1/T^{1/2}$ trend (Klemens *et al.* 1962; Xu *et al.* 2004; Dalton *et al.* 2013; Chang *et al.* 2017; Section 3.2). Importantly, all measurements have been obtained using the same experimental setup and method, resulting in a self-consistent data set. These experiments combine ultrafast optical pump-probe technique with diamond anvil cell, which allows high precision measurements of thermal conductivity at lowermost mantle pressure. Details of experimental procedures and techniques may be found in Dalton *et al.* (2013) and Hsieh *et al.* (2017).

For all samples, lattice thermal conductivity increases with pressure. Note that for pressures larger than 45 GPa and within error bars, conductivity for Bm7.2 remains approximately constant at about 12.9 $W\,m^{-1}\,K^{-1}$. At ambient pressure MgO is thermally more conductive than $MgSiO_3$ by about an order of magnitude. As pressure increases, the absolute difference between the conductivities of these two minerals increases, but the relative difference remains constant at about one order of magnitude. Up to a pressure of 50 GPa, and within measurements error bars, iron has no or very small effects on the conductivity of bridgmanite. At larger pressure, the presence of iron reduces the conductivity of bridgmanite, in response to pressure-induced lattice distortion on iron sites (Hsieh *et al.* 2017). As a result, at 120 GPa, the conductivity for Bm7.2 is reduced by a factor 2 compared to that of $MgSiO_3$. Interestingly, the presence of aluminum strongly moderate this decrease. For instance, the conductivity measured for Al-Bm12.9 is slightly larger than that of Bm7.2. Iron also strongly reduces the thermal conductivity of ferropericlase. For instance, the thermal conductivity for Fp8 is around 5 $W\,m^{-1}\,K^{-1}$ at ambient pressure, and about 50 $W\,m^{-1}\,K^{-1}$ at 120 GPa. Compared to these values, the conductivity of pure MgO is one order of magnitude larger at ambient pressure, and the linear extrapolation of Dalton *et al.* (2013) data to 120 GPa is larger by about a factor 5.5. In addition, for Fp56 conductivity sharply decreases by ∼10 $W\,m^{-1}\,K^{-1}$ around 55 GPa, a drop due to the spin transition of iron (Hsieh *et al.* 2018).

To date, only few additional experimental measurements of thermal conductivities of lower mantle minerals are available. The data we use for pure $MgSiO_3$ (Hsieh *et al.* 2017) are in good agreement with the measurements of Ohta *et al.* (2012), which were performed up to 140 GPa, and with *ab initio* calculations of Dekura *et al.* (2013) at 300 K. Goncharov *et al.* (2015) measured thermal conductivity for Fp10 up to 47 GPa. Below 20 GPa, these data are in very good agreement with those of Hsieh *et al.* (2018), which we use here, but at larger pressure they predicted substantially higher conductivities. Recently, Ohta *et al.* (2017) performed experiments for Fp19, and observed a sharp reduction in conductivity between 20 and 40 GPa. This decrease was attributed to iron spin transition, despite the fact that this transition is usually reported at higher pressure, typically in the range 40–60 GPa. As a result, Ohta *et al.* (2017) measurements for Fp19 are consistent with the experimental data of Hsieh *et al.* (2018) up to 20 GPa, but at pressure larger than 40 GPa they are systematically lower than the conductivity obtained by Hsieh *et al.* (2018) for Fp56.

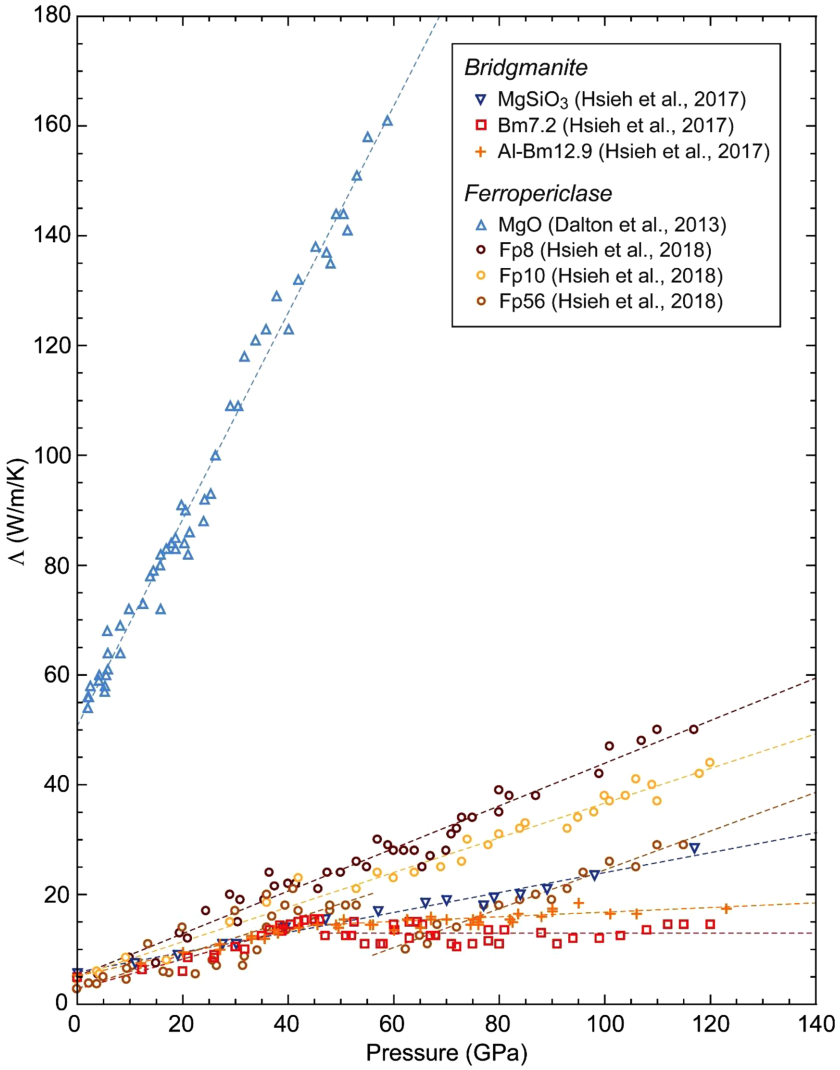

Figure 1. Data set used for the modelling of lower mantle thermal conductivity. All measurements are performed at room temperature. Dashed lines denote the best fitting linear parametrizations for each sample (Table 1).

3 DATA MODELLING

Our modelling of lower mantle thermal conductivity includes three steps. First, we perform high pressure extrapolations individually for each mineral composing the aggregate (here, bridgmanite and ferropericlase) following parametrizations built from our experimental data set. We then correct these high pressure values for the effects of iron and temperature. Finally, we calculate the thermal conductivity of the aggregate by averaging the individual conductivities of bridgmanite and ferropericlase following an appropriate averaging scheme. These operations are detailed below.

3.1 Pressure parametrization

For each sample in our data set, measurements allow us to reconstruct the pressure dependence of lattice thermal conductivity, Λ. Interestingly, experimental data fit well along linear relationships,

$$\Lambda(P) = a_0 + a_1 P. \quad (1)$$

For each sample, the best fitting parameters of eq. (1) are listed in Table 1, and the best-fitting parametrization is represented by dashed lines in Fig. 1. To determine the radial profile of thermal conductivity as a function of depth, we then use the pressure-to-depth function of PREM (Dziewonski & Anderson 1981). Note that for MgO, data are available only up to 60 GPa. To model thermal conductivity of MgO at lowermost mantle pressure, we thus assume that the parametrization built from these data can be extrapolated to higher pressure. Departure from this extrapolation may bias the estimated thermal conductivity of ferropericlase samples with x_{Fe}^{Fp} lower than 0.08, and thus the mantle aggregate conductivity. In practise, however, this case never occurs, since for values of iron partitioning relevant to the lower mantle x_{Fe}^{Fp} never falls below 0.1 (Section 3.3 and Fig. 2).

Table 1. Pressure dependence of thermal conductivity. Experimental data at ambient temperature from various samples are parametrized following $\Lambda(P) = a_0 + a_1 P$.

Mineral	Symbol	Pressure (GPa)	a_0 (W m^{-1} K^{-1})	a_1 W m^{-1} K^{-1} GPa^{-1})	Reference
Bridgmanite					
$MgSiO_3$	Bm	0–120	5.873	0.181	Hsieh *et al.* (2017)
$(Mg_{0.928},Fe_{0.072})SiO_3$	Bm7.2	0–45	2.721	0.275	Hsieh *et al.* (2017)
		45–120	12.906	0.0	
$(Mg_{0.886},Fe_{0.129})(Al_{0.115}Si_{0.906})O_3$	Al-Bm12.9	0–45	5.217	0.206	Hsieh *et al.* (2017)
		45–120	12.597	0.042	
Ferropericlase					
MgO	Per	0–60	50.645	1.878	Dalton *et al.* (2013)
$(Mg_{0.92},Fe_{0.08})O$	Fp8	0–120	5.033	0.388	Hsieh *et al.* (2018)
$(Mg_{0.90},Fe_{0.10})O$	Fp10	0–120	4.959	0.316	Hsieh *et al.* (2018)
$(Mg_{0.44},Fe_{0.56})O$	Fp56	0–55	2.732	0.310	Hsieh *et al.* (2018)
		55–120	–11.189	0.356	

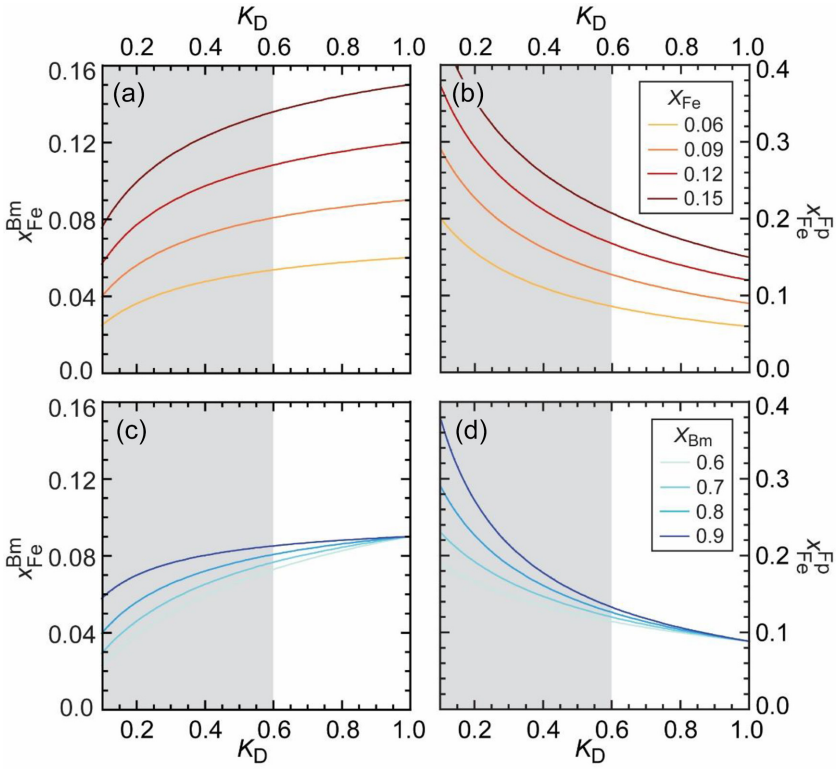

Figure 2. Fractions of iron in bridgmanite, x_{Fe}^{Bm} (left-hand column), and ferroperriclase, x_{Fe}^{Fp} (right-hand column), as a function of the iron partitioning, K_D, and for several values of the global iron content, X_{Fe} (top row, with X_{Bm} fixed to 0.8), and fraction of bridgmanite, X_{Bm} (bottom row, with X_{Fe} fixed to 0.09). The grey areas denote the range of possible values of K_D in the lower mantle (Badro 2014; Piet *et al.* 2016). For mantle aggregate, X_{Bm} and X_{Fe} are typically in the ranges 0.7–0.9 and 0.06–0.13, respectively.

3.2 Effect of temperature

Lattice thermal conductivities of lower mantle mineral decrease with increasing temperature following

$$\Lambda(T) \propto \frac{K}{T^n}, \tag{2}$$

where K is a function of pressure that depends on the material and its iron content. The exponent n depends on the mechanisms controlling the lattice heat transport and is typically between $n = 0.5$ for (Fe,Al)-bearing minerals, in which heat transport is dominated by three-phonon scattering at low phonon frequency, and $n = 1.0$ for $MgSiO_3$, in which heat transport is mostly operated through anharmonic three-phonon scattering (Klemens *et al.* 1962; Xu *et al.* 2004; Dalton *et al.* 2013). Based on experiments at pressures and temperatures up to 26 GPa and 1250 K, respectively, Manthilake *et al.* (2011) found that the conductivities of iron bearing bridgmanite and periclase depend only weakly on temperature, with n around 0.1–0.2. Recent *ab initio* calculations (Stackhouse *et al.* 2015) suggest that, due to saturation effects, the temperature dependence of $MgSiO_3$ at lowermost mantle conditions may be weaker than $1/T$. Here, since the lower mantle minerals are

(Fe,Al)-borne, we modelled lowermost mantle thermal conductivity assuming that the temperature-dependence of thermal conductivities of individual mineral follows eq. (2) with $n = 0.5$. Larger values of n would increase the thermal contribution to variations in thermal conductivity, while smaller values would reduce it. Note, however, that when compositional effects are also taken into account, thermal conductivity anomalies and the corresponding CMB heat flux obtained for $n = 0.5$ and $n = 1.0$ are very similar (Hsieh *et al.* 2017, Sections 5.2 and 5.3).

3.3 Effect of composition

In our modelling, compositional changes in thermal conductivity include two sources: variations due to changes in the mineralogical composition of the aggregate, here the relative fractions of bridgmanite and ferropericlase, X_{Bm} and $X_{\mathrm{Fp}} = (1–X_{\mathrm{Bm}})$; and variations due to changes in the iron fraction of each of these two minerals, x_{Fe}^{Bm} and x_{Fe}^{Fp}, which can be estimated from our experimental data set. In the Earth's mantle, variations in iron are usually parametrized in terms of the global volume fraction of iron oxide (FeO), X_{Fe}, defined as

$$X_{Fe} = X_{Bm}\, x_{Fe}^{Bm} + (1 - X_{Bm})\, x_{Fe}^{fp}. \tag{3}$$

In addition, iron is distributed between bridgmanite and ferropericlase according to the iron partitioning coefficient,

$$K_D = \frac{x_{Fe}^{Bm} / \left(1 - x_{Fe}^{Bm}\right)}{x_{Fe}^{Fp} / \left(1 - x_{Fe}^{Fp}\right)}. \tag{4}$$

Individual fractions of iron in bridgmanite and ferropericlase can be calculated by solving simultaneously eqs (3) and (4) with prescribed values of X_{Fe}, X_{Bm} and K_{D}. Full expressions of these fractions are given in the Appendix (eqs A1 and A2), and Fig. 2 plots them as a function of K_{D} and for several values of X_{Fe} and X_{Bm}. In the Earth's lower mantle, iron preferentially partitions into ferropericlase, implying $K_{\mathrm{D}} < 1$. High pressure mineral physics experiments and *ab initio* calculations further indicate that K_{D} ranges between 0.1 and 0.5 depending on depth and Fe^{3+} content (Badro 2014). Irifune *et al.* (2010) reported values of K_{D} up to 0.8 at the top of the lower mantle, but at pressure larger than 60 GPa (i.e. deeper than ∼1400 km) they found that K_{D} remains constant around 0.4. In addition, recent experiments for aluminum-bearing minerals (Piet *et al.* 2016) obtained K_{D} in the range 0.4–0.6 throughout the lower mantle. For a pyrolitic mantle, in which $X_{\mathrm{Fe}} = 0.09$ and $X_{\mathrm{Bm}} = 0.8$, and assuming $K_{\mathrm{D}} = 0.4$, Fig. 2 indicates that $x_{Fe}^{Bm} = 0.072$ and $x_{Fe}^{Fp} = 0.162$. In the lowermost mantle, LLSVPs may be enriched in iron and in bridgmanite by a few per cent (Trampert *et al.* 2004; Deschamps *et al.* 2012; Mosca *et al.* 2012). Taking $X_{\mathrm{Fe}} = 0.12$ and $X_{\mathrm{Bm}} = 0.9$, the individual fractions of iron in bridgmanite and ferropericlase rise to $x_{Fe}^{Bm} = 0.108$ and $x_{Fe}^{Fp} = 0.232$, respectively. Overall, for conservative ranges of lower mantle values of compositional parameters, $0.1 \leq K_{\mathrm{D}} \leq 0.6$, $0.06 \leq X_{\mathrm{Fe}} \leq 0.13$ and $0.7 \leq X_{\mathrm{Bm}} \leq 0.9$, which also account for their possible lateral variations, the iron fractions in bridgmanite and ferropericlase should fit in the ranges $0.02 \leq x_{Fe}^{Bm} \leq 0.12$ and $0.1 \leq x_{Fe}^{Fp} \leq 0.4$.

To calculate the thermal conductivities of bridgmanite and ferropericlase at a fixed depth and for given values of x_{Fe}^{Bm} and x_{Fe}^{Fp}, we performed simple linear interpolations between the parametrizations listed in Table 1,

$$\Lambda_i \left(x_{Fe}^{i}\right) = \Lambda_0 + a_i x_{Fe}^{i}, \tag{5}$$

where subscripts and superscripts i stand either for bridgmanite or ferropericlase, and parameters Λ_0 and a_i depend on the pressure and are different for different iron fractions. For instance, in the case of ferropericlase with iron fraction between 0.1 and 0.56, Λ_0 is given by the parametrization for Fp10, Λ_{Fp10}, and a_{Fp} is equal to $(\Lambda_{Fp56} - \Lambda_{Fp10})/0.46$, where Λ_{Fp56} is obtained from the parametrization for Fp56. A potential problem with this approach is that calculating conductivities for aggregates with $x_{Fe}^{Bm} > 0.13$ and/or $x_{Fe}^{Fp} > 0.56$ would require extrapolating experimental data, which may bias the results. Practically, however, such high values of x_{Fe}^{Bm} and x_{Fe}^{Fp} never happen for lower mantle values of compositional parameters X_{Bm}, X_{Fe} and K_{D} (Fig. 2), expect, maybe, in ultra-low seismic velocity zones (ULVZs, Mao *et al.* 2006; Wicks *et al.* 2010; Hsieh *et al.* 2018). Another potential problem is that eq. (5) does not account for potential saturation and threshold effects. We discuss this issue more in details in Section 4.

3.4 Estimators for mantle aggregate thermal conductivity

A difficulty in estimating physical and thermochemical properties of a multiphase system is to choose an appropriate averaging scheme to calculate the bulk properties from the individual properties of the phases composing this system. Different schemes may lead to significant differences in estimated properties, in particular when the individual properties of each phase differ by one order of magnitude or more. In addition, the distribution of phases within the aggregate may strongly influence the properties of the aggregate, and most particularly transport properties. If, for instance, grains of one specific phase are interconnected to form a network, the properties of this phase may dominate the properties of the aggregate. In the case of viscosity, interconnected weak phases may lead to weak layers that dominate the deformation of the aggregate. Similarly, thermal conductivity may be dominated by the most conductive phase if the grains of this phase form a network. While an accurate determination of aggregate properties requires additional knowledge on the grains distribution, upper and lower bounds of these properties may be estimated. Hashin–Shtrikman (HS) bounds are based on variational principles and represent the narrowest possible bounds

for a multiphase system (Hashin & Shtriktman 1962). Importantly, HS bounds were specifically calculated to estimate magnetic permeabilities of a multiphase aggregate, but the mathematical treatment used to derive them also applies to other properties, including thermal conductivity.

To identify the best averaging scheme, we calculated five estimators based, respectively, on the arithmetic, geometric, harmonic and Voigt-Reuss-Hill (VRH) averages of the conductivities of bridgmanite and ferropericlase, and on the geometric average of the HS bounds of the conductivities of these minerals. We then compared these estimators with the lower (HS^-) and upper (HS^+) HS bounds. Averaging schemes that do not fit within HS bounds should be rejected. The geometric average of HS bounds automatically fits within these bounds. By contrast, other schemes may be biased towards HS^- or HS^+ or fall outside these bounds, as in the case of electrical conductivity (Khan & Shankland 2012; Deschamps & Khan 2016). For a two-phase aggregate composed of bridgmanite and ferropericlase, and noting that ferropericlase is more thermally conductive than bridgmanite, the lower and upper HS bounds in thermal conductivity are given by,

$$\Lambda_{HS-} = \Lambda_{Bm}\left[1 + \frac{(1-X_{Bm})\left(\Lambda_{Fp}-\Lambda_{Bm}\right)}{\Lambda_{Bm} + X_{Bm}\left(\Lambda_{Fp}-\Lambda_{Bm}\right)/3}\right] \tag{6}$$

and

$$\Lambda_{HS+} = \Lambda_{Fp}\left[1 - \frac{X_{Bm}\left(\Lambda_{Fp}-\Lambda_{Bm}\right)}{\Lambda_{Fp} - (1-X_{Bm})\left(\Lambda_{Fp}-\Lambda_{Bm}\right)/3}\right], \tag{7}$$

where Λ_{Bm} and Λ_{Fp} are the individual conductivities of bridgmanite and ferropericlase, and X_{Bm} the fraction of bridgmanite. Note that because the thermal conductivities of bridgmanite and ferropericlase differ by less than one order of magnitude, one expects the range encompassed by Λ_{HS-} and Λ_{HS+} to be rather narrow, thus reducing the uncertainty related to averaging. The geometric average of HS bounds in mantle thermal conductivity is then simply given by

$$\Lambda_{HSm} = \sqrt{\Lambda_{HS-}\Lambda_{HS+}}. \tag{8}$$

The VRH scheme is defined as the average of arithmetic and harmonic means (Hill 1963). For an aggregate of bridgmanite and ferropericlase, the VRH averaging in thermal conductivity is

$$\Lambda_{VRH} = \frac{1}{2}\left[X_{Bm}\Lambda_{Bm} + (1-X_{Bm})\Lambda_{Fp} + \frac{\Lambda_{Bm}\Lambda_{Fp}}{(1-X_{Bm})\Lambda_{Bm} + X_{Bm}\Lambda_{Fp}}\right]. \tag{9}$$

VRH averaging is commonly used to calculate the thermo-elastic properties of mantle minerals. For the electrical conductivity, by contrast, VRH average has been shown to be biased towards the lower HS bound (e.g. Khan & Shankland 2012; Deschamps & Khan 2016).

Fig. 3 shows profiles of thermal conductivity for a pyrolitic composition ($X_{Fe} = 0.09$ and $X_{Bm} = 0.8$) and $K_D = 0.4$ for all the five estimators we considered. Conductivities are calculated along an adiabatic temperature profile with potential (i.e. ambient pressure) temperature $T_p = 2000$ K and adiabatic depth-gradient $\alpha = 0.35$ K km^{-1}. Fig. 4 plots variations in thermal conductivities with temperature, composition and iron partitioning for the geometric average of HS bounds, at pressure and real (i.e. adiabatically corrected) reference temperature of $P = 120$ GPa and $T_r = 3000$ K, respectively. In both Figs 3 and 4, the ranges covered by HS bounds are indicated by coloured areas. As expected, these range are narrow, around 0.4 W m^{-1} K^{-1} for the aggregate of Fe-bridgmanite and ferropericlase, and less than 0.2 W m^{-1} K^{-1} for the aggregate of (Fe,Al)-bridgmanite and ferropericlase. Several conclusions may be drawn from Figs 3 and 4. First, none of the estimators we tested provide values of aggregate conductivity within HS bounds, except the geometric average of these bounds, which naturally satisfies this requirement (Fig. 3). Geometric and VRH average conductivities are slightly lower than HS^-, while harmonic and arithmetic averages lead to conductivities that are respectively smaller than HS^- and larger than HS^+ by about 0.3 W m^{-1} K^{-1} at the bottom of the mantle. These differences remain modest compared to uncertainties in the measurements, or to the changes induced by temperature or composition. In other words, the mode of averaging affects only slightly estimates of lower mantle thermal conductivity in comparison to other sources of uncertainties and errors. For consistency, we chose to use the geometric average of HS bounds, Λ_{HSm}, to model lower mantle thermal conductivity. With this averaging scheme, mantle conductivity for a pyrolitic model along an adiabat with $T_p = 2000$ K, leading to a real temperature of about 3000 K at the bottom of the mantle, is equal to ~8.6 W m^{-1} K^{-1}.

Secondly, Fig. 4 allows us to estimate changes in thermal conductivity in the lowermost mantle triggered by variations in temperature and composition expected therein. For lateral temperature anomalies around 500 K, thermal conductivity changes by ~1 W m^{-1} K^{-1} (Fig. 4a). Variations in X_{Fe} of 3–4 per cent and in X_{Bm} of 10 per cent trigger changes in thermal conductivity of 1 and 0.8 W m^{-1} K^{-1}, respectively (Figs 4b and c), *i.e.* similar to the effects of temperature. By contrast, the iron partitioning K_D has a small to moderate influence on conductivity (Fig. 4d). Increasing K_D from 0.1 to 0.6 decreases conductivity by 0.5 W m^{-1} K^{-1}. As K_D further increases to 0.8, conductivity changes by another 0.2 W m^{-1} K^{-1}. Our modelling further shows that, compared to temperature and composition, the iron spin transition in ferropericlase has only a minor influence on mantle thermal conductivity. More precisely, the red dashed curve in Fig. 3 and orange curves in Fig. 4, which were calculated by switching off the iron spin transition, indicate that in the mid-lower mantle, around 1400 km, neglecting this transition results in a slight increase in conductivity, by about 0.1 W m^{-1} K^{-1}, while in the lowermost mantle, the difference between the cases with and without the iron spin transition is even smaller, around 0.05 W m^{-1} K^{-1}. This difference increases with increasing X_{Fe} and decreasing X_{Bm} and K_D, but remains limited, up to 0.15 W m^{-1} K^{-1} at 120 GPa and low K_D (Fig. 4d).

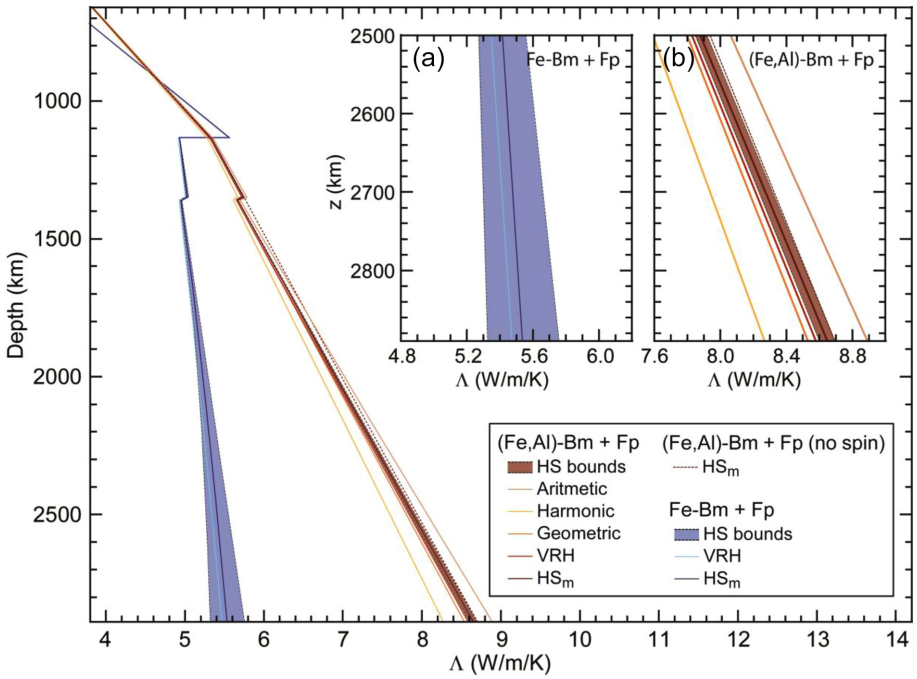

Figure 3. Horizontally average profiles of thermal conductivity in the lower mantle for aggregates of (Fe,Al)-bridgmanite and ferropericlase [(Fe,Al)-Bm + Fp, red and orange curves], and Fe-bridgmanite and ferropericlase (Fe-Bm + Fp, blue curves). All calculations are made along an adiabat with surface (potential) temperature $T_p = 2000$ K and adiabatic gradient 0.35 K km^{-1}. Global iron fraction and volume fraction of bridgmanite are $X_{Fe} = 0.09$ and $X_{Bm} = 0.8$, respectively, and the iron partitioning is $K_D = 0.4$. For each aggregate, colored areas cover values of conductivity within Hashin–Shtrikman (HS) bounds. For the (Fe,Al)-Bm + Fp aggregate, five estimators are shown, and the dark red dashed curve is built by neglecting the spin transition in ferropericlase. For the Fe-Bm + Fp aggregate, only the Voigt–Reuss–Hill average and geometric average of HS bounds are plotted. Plots (a) and (b) in insert show zooms of the conductivity for each aggregate in the depth range 2500–2890 km.

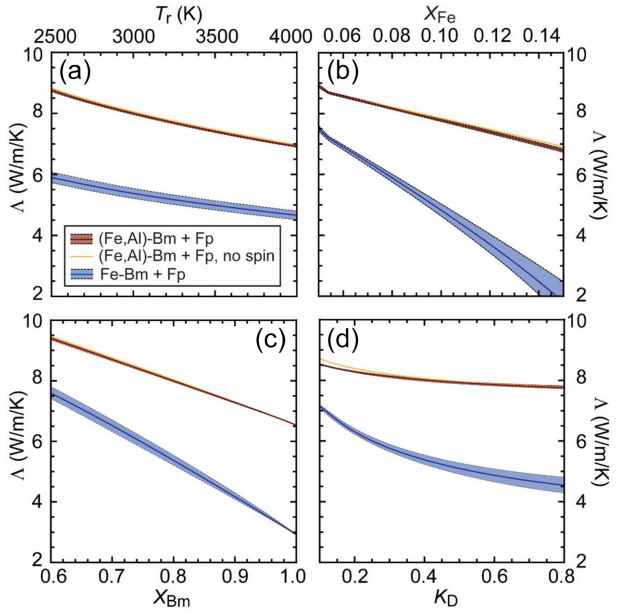

Figure 4. Variations of thermal conductivity with (a) 'real' temperature T_r, (b) global iron fraction X_{Fe}, (c) volume fraction of bridgmanite X_{Bm} and (d) iron partitioning K_D. Two aggregates are considered, (Fe,Al)-bridgmanite plus ferropericlase (red curves and areas), and Fe-bridgmanite plus ferropericlase (blue curves and areas). Curves plot geometric average of Hashin–Shtrikman (HS) lower and upper bounds, and coloured areas denote the area encompassed by these bounds. The orange curves show a case without the spin transition in the ferropericlase and using (Fe,Al)-bridgmanite and ferropericlase data. Default parameters are $T_r = 3000$ K, $X_{Fe} = 0.09$, $X_{Bm} = 0.8$ and $K_D = 0.4$, and all calculations are done at pressure $P = 120$ GPa.

Finally, Figs 3 and 4 indicate that conductivities obtained with Fe-bridgmanite and (Fe-Al)-bridgmanite data strongly differ. At pressure smaller than 45 GPa (depths shallower than 1100 km), both estimates are similar. At larger pressures, however, conductivities obtained with Fe-bridgmanite are substantially smaller than those inferred from (Fe-Al)-bridgmanite data. The difference between these two estimates increases with depth and reaches 3 $W\,m^{-1}\,K^{-1}$ at the bottom of the mantle. Note that when using Fe-bridgmanite, the HS bounds of the aggregate conductivity are wider, and that the VRH average now fits within these bounds (Fig. 3). Furthermore, the influences of compositional parameters (X_{Fe} and X_{Bm}) and iron partitioning are stronger (blue curves in Figs 4b-d). For instance, conductivity decreases by 2.2 $W\,m^{-1}\,K^{-1}$ if X_{Fe} rises by 4 per cent, and by 2.0 $W\,m^{-1}\,K^{-1}$ if K_D changes from 0.1 to 0.6. To estimate mantle thermal conductivity, we chose to use only data for (Fe,Al)-bridgmanite data. This choice is motivated by the observations that Al-bearing bridgmanite is present in mantle aggregate and may influence the iron partitioning (Piet *et al.* 2016).

3.5 Relative anomalies in thermal conductivity

Variations of temperature and composition (parametrized here with the fraction of bridgmanite, X_{Bm}, and the global fraction of iron, X_{Fe}) at a given depth result in lateral variations in thermal conductivity. These anomalies may be measured relatively to a reference conductivity defined at a reference thermochemical state, which may be defined as the horizontally averaged mantle temperature, T_{ref}, and composition, $X_{Bm,ref}$ and $X_{Fe,ref}$, at this depth.

The relative variations of thermal conductivity with respect to temperature can be easily calculated by deriving eq. (2), leading to

$$\mathrm{dln}\,\Lambda^T = \frac{1}{\Lambda_{ref}}\frac{\partial\Lambda}{\partial T}\mathrm{d}T = -n\frac{\mathrm{d}T}{T}, \tag{10}$$

where $\mathrm{d}T = (T—T_{ref})$ is the lateral temperature anomaly compared to a reference temperature T_{ref}, and Λ_{ref} the conductivity at temperature T_{ref}. At the bottom of the mantle, this average temperature may range between 3000 and 4000 K (e.g. Tackley 2012), while probabilistic tomography (Trampert *et al.* 2004; Mosca *et al.* 2012) suggests temperature anomalies up to 400 K in amplitude. Taking $n = 0.5$ and $\mathrm{d}T = 400$ K, thermal conductivity should vary by up to 5–7 per cent, compared to its horizontal average.

The aggregate conductivity depends explicitly on X_{Bm}, as indicated by eqs (6)–(8), and implicitly on both X_{Bm} and X_{Fe} through the expressions of x_{Fe}^{Bm} and x_{Fe}^{Fp} (eqs A1 and A2). The detailed expression of relative anomalies in aggregate conductivity with respect to X_{Bm} and X_{Fe} further depends on the assumed averaging scheme. For instance, Hsieh *et al.* (2017) inferred relative anomalies for the VRH average from eq. (9). Relative anomalies in the geometric average of HS bounds, $\mathrm{dln}\Lambda_{HSm}^{Bm}$ and $\mathrm{dln}\Lambda_{HSm}^{Fe}$, can be derived from eqs (6) to (8) and are detailed in Appendix (eqs A3 and A4). The total compositional effect is then simply given by the sum of these anomalies, that is

$$\mathrm{dln}\,\Lambda_{HSm}^{C} = \mathrm{dln}\Lambda_{HSm}^{Bm} + \mathrm{dln}\Lambda_{HSm}^{Fe}. \tag{11}$$

Fig. 5 plots relative anomalies in thermal conductivity due to variations in composition at $P = 120$ GPa, and for $K_D = 0.4$ and a pyrolitic reference composition, that is $X_{Bm,ref} = 0.8$ and $X_{Fe,ref} = 0.09$. Note that because x_{Fe}^{Bm} and x_{Fe}^{Fp} depend on both X_{Bm} and X_{Fe}, relative anomalies in aggregate conductivity with respect to iron, $\mathrm{dln}\Lambda_{HSm}^{Bm}$ (eq. A3), and bridgmanite, $\mathrm{dln}\Lambda_{HSm}^{Fe}$ (eq. A4), also depend on both X_{Bm} and X_{Fe} (plots a and b in Fig. 5). For instance, an excess of iron of 4 per cent triggers a decrease in aggregate conductivity of ∼10 per cent at $X_{Bm} = X_{Bm,ref}$, and this reduction is slightly enhanced as the aggregate gets enriched in bridgmanite. Similarly, an enrichment in bridgmanite by 10 per cent reduces the aggregate conductivity by ∼10 per cent. Combined enrichments in iron by 4 per cent and bridgmanite by 10 per cent thus induce a decrease in thermal conductivity by 20 per cent compared to its reference value (Fig. 5c). Similar results are obtained using a VRH averaging scheme (Fig. 5d).

4 SATURATION AND THRESHOLD EFFECTS

To model the impact of iron on mantle thermal conductivity, we interpolated individual conductivities of bridgmanite and ferropericlase between available measurements with different iron fractions. A potential bias of this approach is that it does not account for possible saturation and threshold effects. To date, available experimental data do not allow fixing the iron content at which saturation and threshold occur, if they occur at all. However, general trends can be outlined.

Saturation effects alter the thermal conductivity estimated from linear interpolation (or extrapolation) differently depending on the iron fraction $x_{Fe,sat}$ at which saturation starts operating. If $x_{Fe,sat}$ fits between two experimentally measured points, x_1 and x_2 (Fig. 6a), the conductivity measured at x_2 is the saturated value of thermal conductivity. Accounting for saturation effects would then lead to values of the conductivity lower or equal to those obtained by linear interpolation of experimental data if $x_{Fe} \leq x_2$, and larger than the extrapolated values in the opposite case. If $x_{Fe,sat}$ is larger than the highest iron content at which experiments were performed (Fig. 6b), saturation has more complex consequences, leading to conductivity values either lower or larger than the value extrapolated from experimental data, depending on the exact value of $x_{Fe,sat}$. This case is, however, unlikely, since in the lower mantle x_{Fe}^{Bm} and x_{Fe}^{Fp} are expected to remain lower than 0.12 and 0.4, respectively (Fig. 2), that is lower than the iron fractions of experimental samples of our data set. Exceptions may occur locally in ULVZs, if these regions are strongly enriched in iron (Mao *et al.* 2006; Wicks *et al.* 2010). Thermal conductivity within ULVZs would then be strongly reduced by an amount that decreases with decreasing $x_{Fe,sat}$ (Hsieh *et al.* 2018). Here, we focus on the case $x_1 \leq x_{Fe,sat} \leq x_2$ (Fig. 6a), which is *a priori* representative of the regular mantle and LLSVPs.

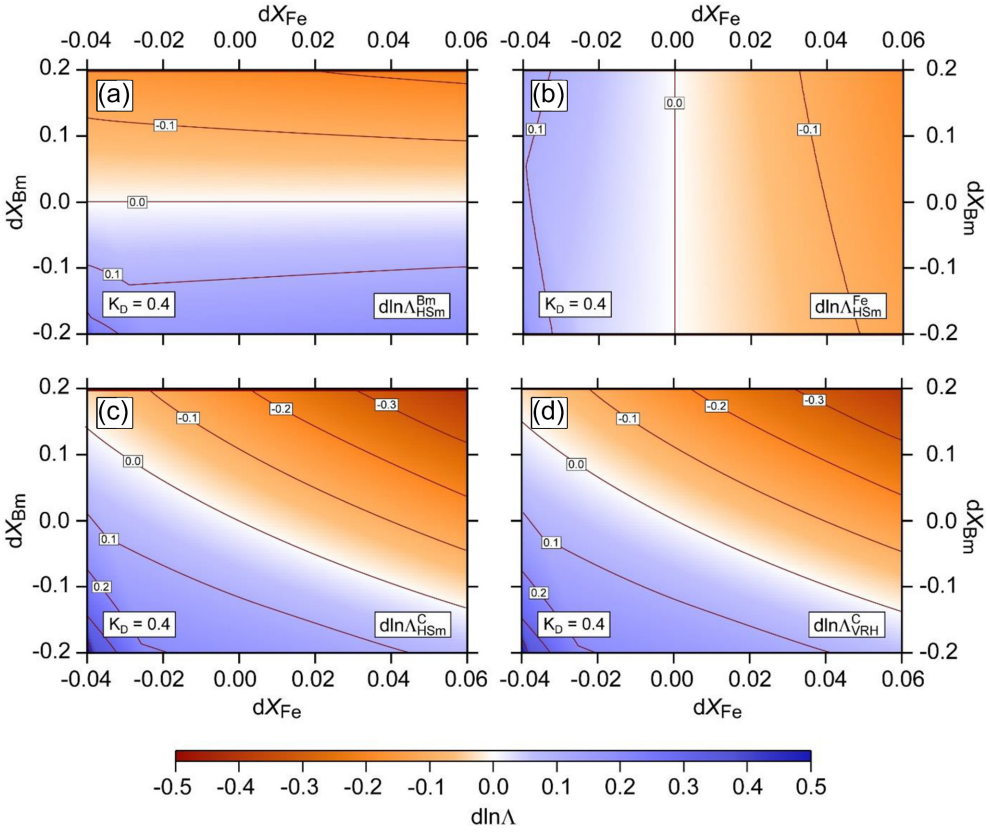

Figure 5. Relative anomalies in thermal conductivity of an aggregate of bridgmanite and ferropericlase induced by anomalies in the global iron fraction, dX_{Fe}, and in the volume fraction of bridgmanite, dX_{Bm}. All calculations are done at $P = 120$ GPa, real temperature $T_r = 3000$ K and iron partitioning $K_D = 0.4$. The reference composition is $X_{Bm,ref} = 0.8$ and $X_{Fe,ref} = 0.09$. In plots (a) to (c), the aggregate conductivity is estimated from the geometric average of Hashin–Shtrikman bounds. (a) Relative anomalies with respect to fraction of bridgmanite (eq. A3). (b) Relative anomalies with respect to iron content (eq. A4). (c) Cumulated relative anomalies with respect to iron and bridgmanite fractions (eq. 11). (d) Cumulated relative anomalies with respect to iron and bridgmanite fractions assuming a VRH average for the aggregate conductivity [see Hsieh *et al.* (2017) for relationships equivalent to eqs (A3) and (A4)].

Fig. 7(a) shows saturation effects as a function of the global iron fraction X_{Fe} for several cases. Saturation in the conductivity of ferropericlase (blue curves in Fig. 7a) induces a moderate reduction in mantle thermal conductivity, compared to the values inferred from linear interpolation of experimental data (red curve in Fig. 7a). For $x^{Fp}_{Fe,sat} = 0.1$, which is the lowest possible value of $x^{Fp}_{Fe,sat}$, this reduction is about 0.6 W m^{-1} K^{-1} at $X_{Fe} = 0.06$, and it decreases to 0.4 W m^{-1} K^{-1} at $X_{Fe} = 0.14$. Saturation in the conductivity of bridgmanite (green curves in Fig. 7a) triggers more substantial changes. Fixing $x^{Bm}_{Fe,sat} = 0.05$, for instance, reduces mantle conductivity by 1.6 W m^{-1} K^{-1} at $X_{Fe} = 0.06$, and 0.4 W m^{-1} K^{-1} at $X_{Fe} = 0.14$. Accounting for saturation in both bridgmanite and ferropericlase with $x^{Bm}_{Fe,sat} = 0.1$ and $x^{Fp}_{Fe,sat} = 0.15$, leads to a constant mantle conductivity at 6.3 W m^{-1} K^{-1} for all values of X_{Fe} between 0.08 and 0.15. Compared to the value deduced from experimental data, this corresponds to a reduction by 24 and 8 per cent, respectively. Relative changes in thermal conductivity with composition are also affected by saturation effects (Fig. 8). Saturation effects in both bridgmanite and ferropericlase trigger larger relative anomalies in aggregates depleted in iron ($dX_{Fe} < 0$), but slightly smaller anomalies in aggregates enriched in iron ($dX_{Fe} > 0$). For instance, assuming $x^{Bm}_{Fe,sat} = 0.1$ and $x^{Fp}_{Fe,sat} = 0.15$, a combined enrichment in iron by 4 per cent and in bridgmanite by 10 per cent leads to a thermal conductivity anomaly of –18 per cent, instead of –21 per cent in absence of saturation effects. Saturation, depending on the iron content at which it starts operating, may thus slightly reduce our estimates of thermal conductivity anomalies within LLSVPs (Section 5). It should be noted, however, that these changes would be limited, reducing the amplitude of relative anomalies in conductivity, typically by only a few per cent.

Lower mantle minerals may also be subject to threshold effects, where the conductivity initially decreases rapidly and then, upon reaching a threshold value, continues to decrease at a slower rate. Accounting for threshold effects would result in values of the conductivity lower than the value interpolated from experimental data (Fig. 6a). Such reduction is equivalent to a decrease in the slope of the linear regression a_i estimated from experimental data (eq. 5), and can be parametrized by fixing the ratio between the slopes accounting for and neglecting the threshold effects, $\zeta = a_{threshold}/a_i$. Experimental data for ferropericlase (Hsieh *et al.* 2018) indicate that any possible threshold effect with this mineral would occur at x^{Fp}_{Fe} less than 0.08. However, since in the lower mantle x^{Fp}_{Fe} is likely greater than this value (Fig. 2), the consequences of such threshold on the aggregate conductivity would be minimal. By contrast, because the lowest value of x^{Bm}_{Fe} in our experimental data set is equal to 0.129, threshold effects in bridgmanite may affect our calculations. Fig. 7(d) plots conductivity as a function of X_{Fe} for several values of the threshold values, modelled by a reduction in the slope of the linear regression a_{Bm} (eq. 5) between $MgSiO_3$ and (Al,Fe)-bridgmanite.

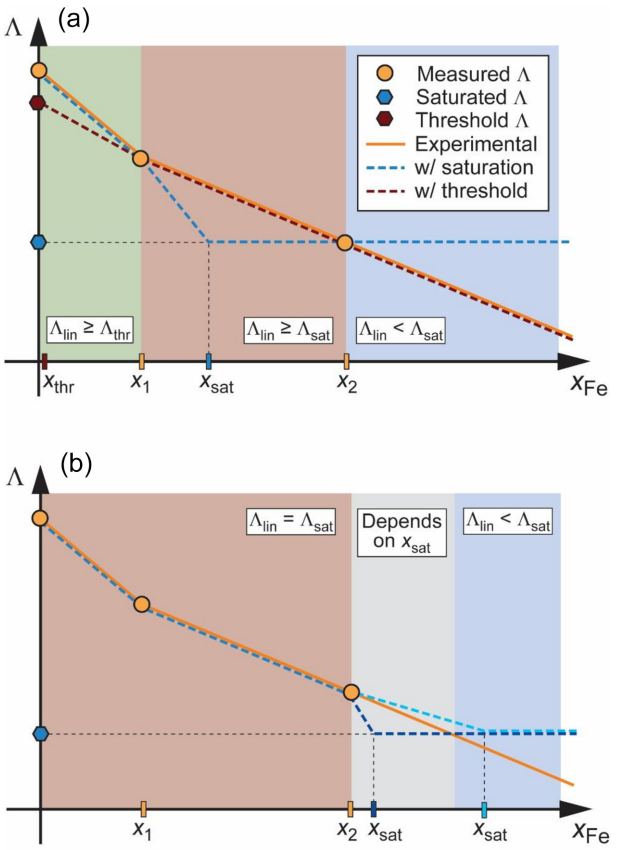

Figure 6. Saturation and threshold effects. (a) Saturation occurs at an iron content x_{sat} intermediate between two experimental samples, x_1 and x_2, and results in values of the conductivity lower than the values interpolated from experimental data if $x_{Fe} \leq x_2$, and larger in the opposite case. Threshold effects also result in values of the conductivity lower than those deduced from experiments. (b) Saturation occurs at an iron content x_{sat} higher than those explored in experiments and results in values of the conductivity either lower or larger than the values extrapolated from experiments, depending on the value of x_{sat}.

The reduction in conductivity increases as the threshold conductivity decreases, but this reduction is less pronounced as X_{Fe} increases. For instance, compared to the value predicted by experimental data and assuming a threshold conductivity corresponding to $\zeta = 0.1$, the aggregate conductivity is reduced by 15 and 5 per cent for $X_{Fe} = 0.08$ and $X_{Fe} = 0.14$, respectively. Accounting for threshold effects further reduces the relative changes in thermal conductivity (Fig. 8d). For $\zeta = 0.5$, the relative anomaly in conductivity triggered by a joint enrichment in iron and bridgmanite of 4 and 10 per cent, respectively, is around –15 per cent, compared to –20 per cent if threshold effects are absent.

Interestingly, both threshold and saturation effects, if operating in lower mantle minerals, would result in a reduction of the aggregate conductivity (Fig. 7) and of its relative variations with compositional parameters (Fig. 8). The lower mantle conductivity and its relative variations with composition we inferred in Section 5.2 may thus be considered as upper bounds. Unfortunately, in absence of constraints from mineral physics experiments, the impact of saturation and threshold effects on mantle thermal conductivity cannot be quantified with precision. Detailed estimates will require additional experiments for bridgmanite with low iron fractions, around 0.05 or less, and ferropericlase with iron fractions between 0.15 and 0.40.

5 APPLICATIONS TO THE LOWERMOST MANTLE

Seismic tomography indicates that the lowermost mantle is strongly heterogeneous at large scale. Several hints suggest that observed seismic features require a combination of lateral variations in both temperature and composition (*e.g.* Ishii & Tromp 1999; van der Hilst and Kárason 1999; Deschamps & Trampert 2003; Trampert *et al.* 2004; Hernlund & Houser 2008), the compositional contribution being well explained by changes in the iron content, X_{Fe}, and in the fraction of bridgmanite, X_{Bm} (Trampert *et al.* 2004; Deschamps *et al.* 2012; Mosca *et al.* 2012). If present in the deep mantle, lateral variations in iron and bridgmanite, together with temperature anomalies, may trigger lateral variations in thermal conductivity that may, in turn, influence the dynamics of the lowermost mantle and the heat transfer at the CMB.

5.1 Thermochemical structure

Inferring maps of the lowermost thermochemical structure from observed seismic structure requires appropriate sensitivities of seismic observables to temperature and composition (e.g. Trampert *et al.* 2001). Maps of density anomalies, inferred from normal modes data (Ishii &

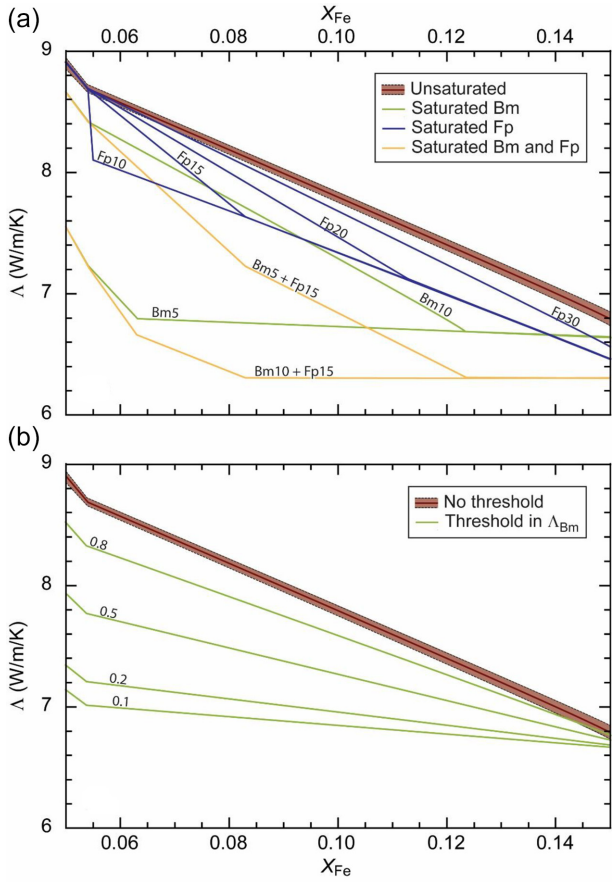

Figure 7. Saturation and threshold effects as a function of the global iron fraction, X_{Fe}. For comparison, coloured areas and red curves represent the unsaturated case (Hashin–Shtrikman bounds and geometric average of these bounds). (a) Saturation effects. Labels on curves indicate the iron fraction in bridgmanite (Bm) and/or ferropericlase (Fp) at which saturation occurs. (b) Threshold effect in bridgmanite, parametrized as a function of the reduction in the slope of the linear regression a_{Bm} (eq. 5) between $MgSiO_3$ and (Al,Fe)-bridgmanite samples. Labels on curve indicate the ratio between the reduced and regular slopes, $\zeta = a_{threshold}/a_{Bm}$. All calculations are made at $P = 120$ GPa, $T_r = 3000$ K, $K_D = 0.4$. The reference composition is $X_{Bm,ref} = 0.8$ and $X_{Fe,ref} = 0.09$, and the aggregate conductivity is estimated from the geometric average of Hashin–Shtrikman bounds.

Tromp 1999; Trampert *et al.* 2004; Mosca *et al.* 2012), provide essential information that complements shear-wave and compressional-wave (or bulk-sound velocity) anomalies. Following Trampert *et al.* (2004), we assumed that compositional changes in the lowermost mantle are dominated by variations in iron and bridgmanite (dX_{Fe} and dX_{Bm}). We considered two possible thermochemical models of the lowermost mantle, hereafter referred to as models TC1 and TC2 (Fig. 9). Model TC1 is obtained by solving the system

$$\begin{cases} d\ln V_S = \dfrac{\partial \ln V_S}{\partial T} dT + \dfrac{\partial \ln V_S}{\partial X_{Fe}} dX_{Fe} + \dfrac{\partial \ln V_S}{\partial X_{Bm}} dX_{Bm} \\ d\ln V_\phi = \dfrac{\partial \ln V_\phi}{\partial T} dT + \dfrac{\partial \ln V_\phi}{\partial X_{Fe}} dX_{Fe} + \dfrac{\partial \ln V_\phi}{\partial X_{Bm}} dX_{Bm} \\ d\ln \rho = \dfrac{\partial \ln \rho}{\partial T} dT + \dfrac{\partial \ln \rho}{\partial X_{Fe}} dX_{Fe} + \dfrac{\partial \ln \rho}{\partial X_{Bm}} dX_{Bm} \end{cases}, \tag{18}$$

where $d\ln V_S$, $d\ln V_\Phi$, and $d\ln \rho$ are the anomalies in shear-wave velocity, bulk-sound velocity and density inferred by Trampert *et al.* (2004), and the functions $\partial \ln X / \partial Y$ are the partial derivatives (sensitivities) of each seismic parameters with respect to temperature, iron, and bridgmanite. Here, we used the sensitivities calculated by Deschamps *et al.* (2012). Due to the radial parametrization used in Trampert *et al.* (2004), model TC1 samples the layer 2000–2891 km. Note that because of restrictions in the measurements of normal modes, both models are limited to even spherical harmonic degrees up to $l = 6$. Compared to the original thermo-chemical model of Trampert *et al.* (2004), thermal anomalies are slightly lower in model TC1, with root-mean-square (rms) around 132 K (Table 2) instead of 183 K, whereas compositional anomalies are stronger, with rms in dX_{Fe} and dX_{Bm} around 1.4 and 7.2 per cent, respectively, instead of 0.9 and 4.3 per cent in Trampert *et al.* (2004). Model TC2 is directly taken from the thermochemical distributions obtained by Mosca *et al.* (2012). It accounts for the possible presence of post-perovskite (pPv) at the bottom of the mantle, and samples a thinner layer, 2750–2891 km, than model TC1.

Due to different vertical parametrizations, models TC1 and TC2 are substantially different in pattern (Fig. 9). Note, however, that both models predict strong enrichment in iron in regions corresponding to LLSVPs. In addition, amplitude of thermal anomalies are slightly larger in model TC2, but still comparable to those of model TC1 (Table 2). A striking difference is that, because it accounts for the presence of

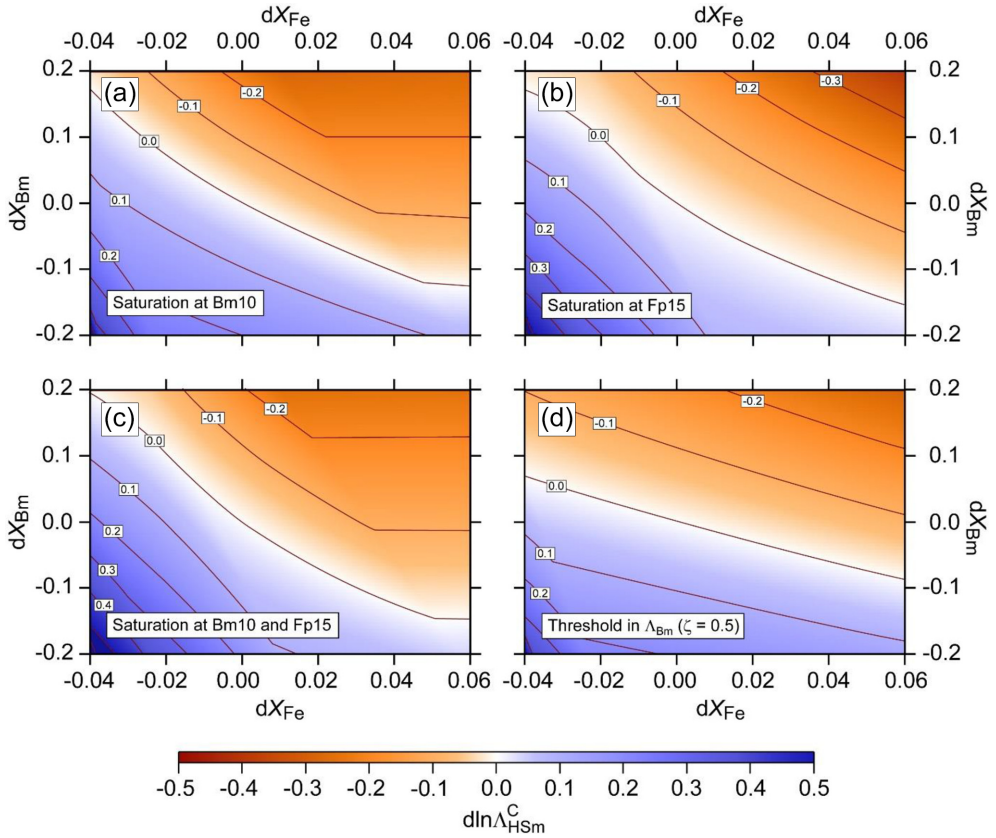

Figure 8. Influence of saturation and threshold effects on relative anomalies in thermal conductivity. (a) (Fe,Al)-bridgmanite saturated at $x_{Fe}^{Bm} = 0.1$. (b) Ferropericlase saturated at $x_{Fe}^{Fp} = 0.15$. (c) (Fe,Al)-bridgmanite and ferropericlase saturated at $x_{Fe}^{Bm} = 0.1$ and $x_{Fe}^{Fp} = 0.15$, respectively. (d) Threshold effect in bridgmanite. The threshold effect is parametrized by a reduction in the linear regression slope a_{Bm} (eq. 5) between $MgSiO_3$ and (Al,Fe)-bridgmanite, with a ratio between the reduced and regular slopes, $\zeta = a_{\mathrm{threshold}}/a_{\mathrm{Bm}}$, fixed to 0.5. Results are plotted as a function of anomalies in the global iron fraction, $\mathrm{d}X_{\mathrm{Fe}}$, and in the volume fraction of bridgmanite, $\mathrm{d}X_{\mathrm{Bm}}$. All calculations are made at $P = 120$ GPa, $T_{\mathrm{r}} = 3000$ K and $K_{\mathrm{D}} = 0.4$. The reference composition is $X_{\mathrm{Bm,ref}} = 0.8$ and $X_{\mathrm{Fe,ref}} = 0.09$, and the aggregate conductivity is estimated from the geometric average of Hashin–Shtrikman bounds.

pPv, model TC2 predicts very small values of $\mathrm{d}X_{\mathrm{Bm}}$, with rms of 0.5 per cent (Table 2). A depletion in pPv, as expected in LLSVPs, and an excess in bridgmanite have similar effects on seismic velocities, that is decreasing shear-wave velocity and increasing bulk-sound velocity. As a result, if lateral variations in the fraction of pPv are accounted for, explaining observed seismic velocity anomalies requires smaller variations in bridgmanite.

5.2 Thermal conductivity maps and implications for deep mantle dynamics

Fig. 10 plots relative variations in thermal conductivity associated with thermochemical models TC1 and TC2 and calculated according to eqs (10), (A3) and (A4). Anomalies inferred from model TC1 are dominated by compositional effects. The rms of relative conductivity anomalies due to changes in X_{Fe} and X_{Bm}, $\mathrm{dln}\Lambda_{HSm}^{Fe}$ and $\mathrm{dln}\Lambda_{HSm}^{Bm}$, are equal to 3.5 and 6.4 per cent (Table 2), respectively, and strongest variations are found in LLSVPs, where iron and bridgmanite excesses reduce thermal conductivity by up to 11 and 15 per cent. Relative anomalies triggered by variations in temperature, $\mathrm{dln}\Lambda^{\mathrm{T}}$, are smaller in amplitude, with an rms of 2.2 per cent. As a result, the total conductivity anomalies, $\mathrm{dln}\Lambda_{\mathrm{HSm}}$, predicted by model TC1 are large, with rms around 10 per cent. Again, the strongest changes, corresponding to a reduction in conductivity of 26 per cent, are found within LLSVPs. By contrast, compared to the variations obtained with model TC1, the $\mathrm{dln}\Lambda_{HSm}^{Bm}$ inferred from model TC2 are very small, whereas $\mathrm{dln}\Lambda_{HSm}^{Fe}$ and $\mathrm{dln}\Lambda^{\mathrm{T}}$ are comparable, with rms of 3.8 and 2.6 per cent, respectively. This results in much smaller $\mathrm{dln}\Lambda_{\mathrm{HSm}}$ with rms of only 2.6 per cent (Table 2). Interestingly, while it reaches only 4.2 per cent, the maximum reduction in thermal conductivity is still located within the LLSVPs (Fig. 10h). Differences in the variations in conductivity predicted by models TC1 and TC2 reflect the structural differences between these models. Differences between patterns of conductivity (Fig. 10) mimic the differences of patterns in temperature, iron and bridgmanite anomalies (Fig. 9), which are partly related to the radial parametrization of models TC1 and TC2. Differences in amplitude mostly result from differences in the distribution of bridgmanite (section 5.1). Because it accounts for possible variations in the stability field of post-perovskite, model TC2 predicts very small variations in bridgmanite. We further explored the effect of the temperature exponent n, controlling the amplitude of conductivity changes with temperature (eq. 2). Reducing n, moderates the influence of temperature changes on conductivity. As one would expect, conductivity changes due to temperature anomalies ($\mathrm{dln}\Lambda^{\mathrm{T}}$) are strongly reduced as n decreases (Table 3). However, the value of n has only a small influence on the total conductivity changes

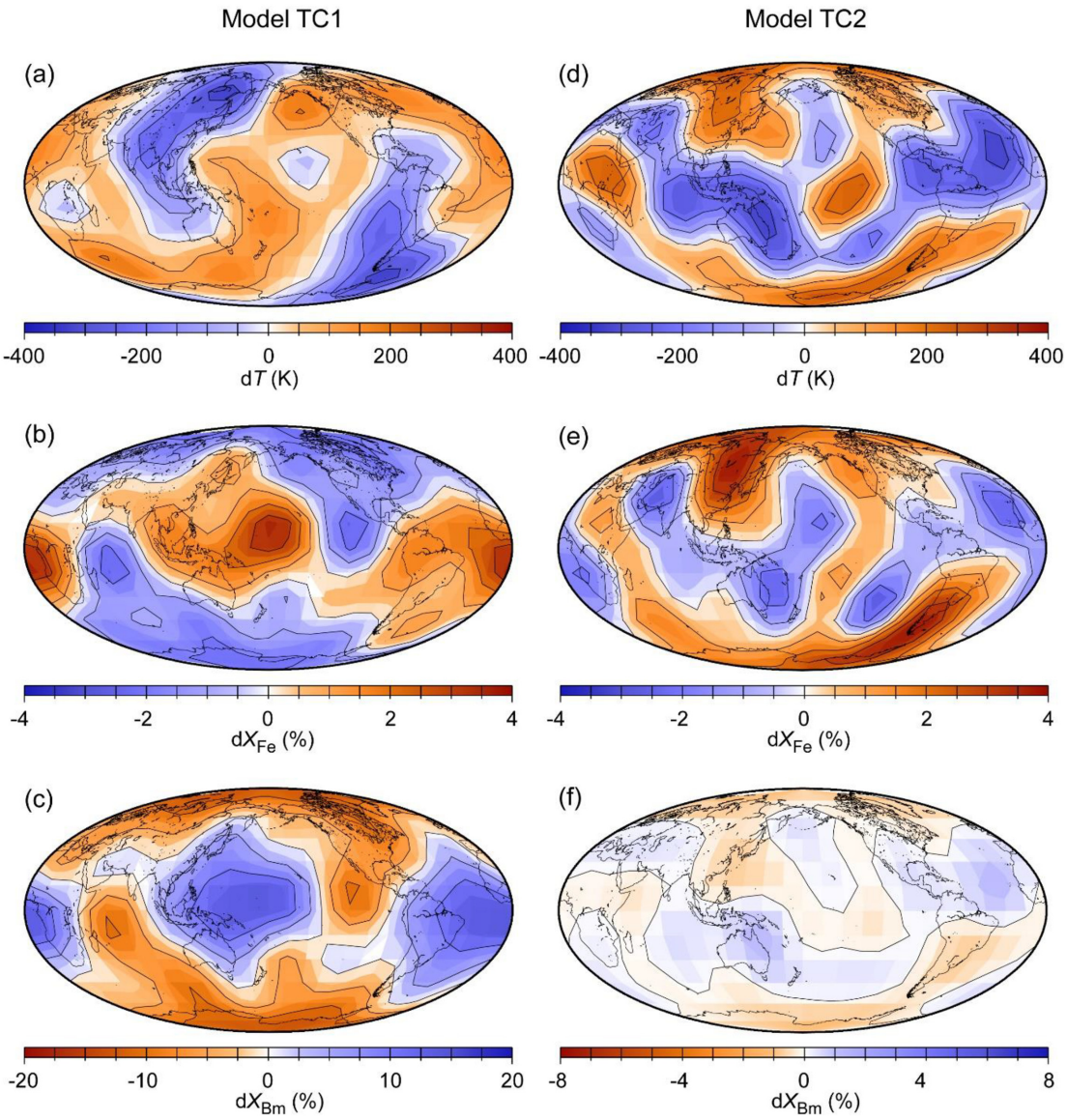

Figure 9. Thermochemical distributions in the lowermost mantle modified from Trampert *et al.* (2004) (model TC1, left-hand column), and from Mosca *et al.* (2012) (model TC2, right-hand column). Thermo-chemical models include anomalies in temperature (a and d), global fraction of iron (b and e), and fraction of bridgmanite (c and f). Model TC1 was built from the seismic distributions of Trampert *et al.* (2004) and seismic sensitivities of Deschamps *et al.* (2012). Model TC2 is directly taken from Mosca *et al.* (2012) and accounts for the presence of post-perovskite at the bottom of the mantle. Both models are horizontally parametrized on a 15° × 15° grid. Vertical resolution is 2000–2891 km for model TC1 and 2750–2891 km for model TC2. Contour levels are 100 K for dT, 1 per cent for dX_{Fe} and 5 per cent for dX_{Bm}.

Table 2. Root mean square (rms), minimum and maximum in thermochemical anomalies from thermochemical models TC1 and TC2 (Fig. 9) and related anomalies in thermal conductivity (Fig. 10) and CMB heat flux (Fig. 11).

Quantity	Model TC1			Model TC2		
	rms	min	max	rms	min	max
Thermochemical anomalies						
dT (K)	131.9	–353.5	206.0	153.1	-337.4	280.6
dX_{Fe} (%)	1.4	–2.5	3.7	1.6	–3.9	2.9
dX_{Bm} (%)	7.2	–12.0	14.6	0.5	–1.2	1.3
Thermal conductivity anomalies						
$\mathrm{d}\ln\Lambda^{\mathrm{T}}$	0.022	–0.034	0.059	0.026	-0.047	0.056
$\mathrm{d}\ln\Lambda^{Fe}_{HSm}$	0.035	–0.106	0.054	0.038	–0.073	0.106
$\mathrm{d}\ln\Lambda^{Bm}_{HSm}$	0.064	–0.149	0.099	0.004	–0.013	0.009
$\mathrm{d}\ln\Lambda_{\mathrm{HSm}}$	0.099	–0.257	0.157	0.026	-0.042	0.070
CMB heat flux anomalies						
$\mathrm{d}\ln\Phi_{\mathrm{dT}}$	0.176	–0.275	0.471	0.204	–0.374	0.450
$\mathrm{d}\ln\Phi_{\mathrm{d}\Lambda}$	0.099	–0.257	0.157	0.026	-0.042	0.070
$\mathrm{d}\ln\Phi$	0.215	–0.416	0.532	0.199	–0.362	0.439

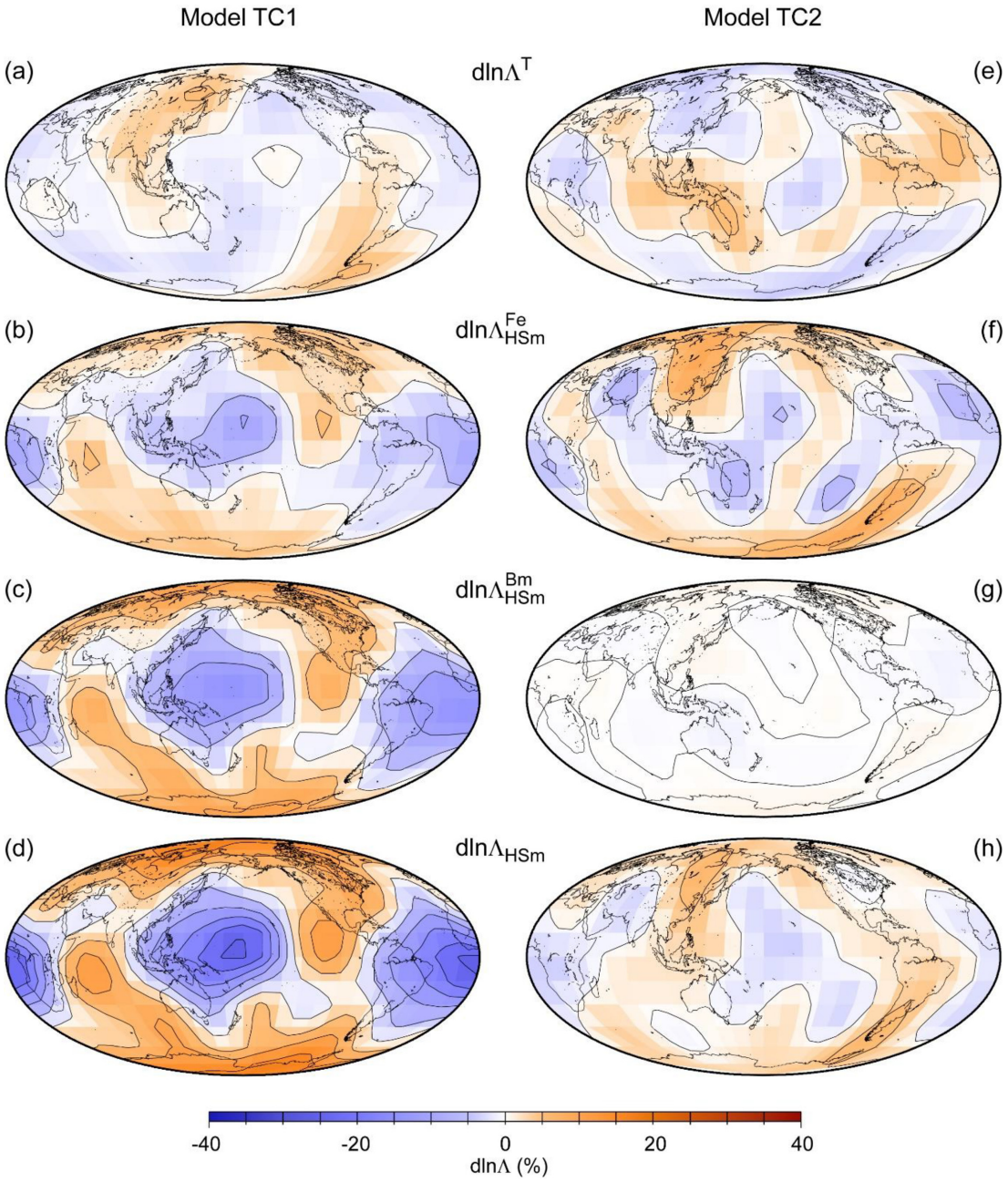

Figure 10. Relative variations in thermal conductivity in the lowermost mantle inferred from thermo-chemical models TC1 (left-hand column) and TC2 (right-hand column). First, second, and third rows plot relative anomalies due to variations in temperature ($d\ln\Lambda_T$, eq. 10), iron content ($d\ln\Lambda^{Fe}_{HSm}$, eq. A4), and fraction of bridgmanite ($d\ln\Lambda^{Bm}_{HSm}$, eq. A3), respectively. The last row plots the total relative anomalies, $d\ln\Lambda_{HSm}$. All calculations are made at $P = 120$ GPa, $T_r = 3000$ K and $K_D = 0.4$. The reference composition is $X_{Bm,ref} = 0.8$ and $X_{Fe,ref} = 0.09$, and the aggregate conductivity is estimated from the geometric average of Hashin–Shtrikman bounds. Horizontal and vertical parametrizations are the same as in Fig. 9. Contour levels are 5 per cent on all plots.

Table 3. Effect of the temperature exponent n (eq. 2) on the variations in lower mantle thermal conductivity (Fig. 10) and CMB heat flux (Fig. 11) estimated from thermochemical model TC1 (Fig. 9).

Quantity		n		
		0.2	0.5	1.0
$d\ln\Lambda^T$	rms	0.009	0.022	0.044
	min	–0.014	–0.034	–0.069
	max	0.026	0.059	0.118
$d\ln\Lambda_{HSm}$	rms	0.098	0.099	0.105
	min	–0.249	–0.257	–0.274
	max	0.145	0.157	0.185
$d\ln\Phi$	rms	0.203	0.215	0.235
	min	–0.404	–0.416	–0.437
	max	0.498	0.532	0.588
q^*		0.451	0.474	0.512

(dlnΛ). For instance, in the case of model TC1, rms in dlnΛ decreases very slightly, from 0.105 to 0.098, when n is varied between 1.0 and 0.2.

An interesting result is that despite their differences, models TC1 and TC2 predict a reduction of thermal conductivity within LLSVPs (Fig. 10). This may, in turn, impact the dynamics of these regions, since a lower conductivity decreases heat transfer by conduction and promotes convection. A reduction by 25 per cent, as expected by model TC1, may reduce heat exchange between LLSVPs and the surrounding mantle and favor internal flow within these structures. However, numerical simulations of thermochemical convection accounting explicitly for variations of conductivity with temperature and composition should, be conducted to quantify this effect. Note that a depth-dependent thermal conductivity is already included in models of thermochemical convection, and helps stabilizing reservoirs of dense material (Tackley 1998). Recent simulations further indicate that it reduces the number of thermal plumes generated outside thermochemical reservoirs and increases their spacing (Li & Zhong 2017).

5.3 Implications for heat flux at CMB

The powering and strength of geodynamo strongly depend on the amount of heat that can be extracted from the core, and thus on the CMB heat flux. The amplitude and lateral variations in this flux may be used as a boundary condition for models of outer core dynamics, influencing in turn the outer core flow and the geomagnetic field it generates. Lateral distribution in CMB heat flux depends on the distribution in thermal conductivity, Λ (φ,θ), and is given by

$$\Phi_{\mathrm{CMB}}\ (\varphi,\theta) = \ \Lambda\,(\varphi,\theta)\,\frac{[T_{CMB} - T\,(\varphi,\theta,D)]}{D}, \tag{19}$$

where φ and θ are the longitude and latitude, T_{CMB} the temperature at CMB, which is assumed constant everywhere on the CMB and $T(\varphi,\theta,D)$ the temperature at location φ, θ and altitude D above the CMB. A difficulty is to choose a relevant value for D. Ideally, since eq. (19) is representing the heat flux right above the CMB, D should be chosen as small as possible, typically a few tens of kilometres. However, tomographic models, from which variations in temperature in the lowermost mantle are deduced, have a limited vertical resolution, typically a few hundreds of kilometres, and temperature anomalies inferred from these models represent a vertical average within this layer. A possible solution to this problem is to fix the value of D to the thickness of the thermal boundary layer at the bottom of the mantle, that is the region where the depth-increase of temperature is superadiabatic. This value is not well constrained, but may reach a few hundred kilometres, allowing self-consistency with the radial parametrization of temperature anomalies inferred from seismic tomography. It is important to note that the value of D does not alter the relative lateral variations in CMB heat flux (eq. 23 below). By contrast, it obviously affects the reference (horizontally averaged) heat flux, and thus the peak-to-peak amplitude of heat flux variations. Taken at reference temperature (defined by the mantle geotherm) and thermal conductivity, T_{ref} and Λ_{ref}, eq. (19) defines a reference heat flux,

$$\Phi_{ref} = \Lambda_{ref}\,\frac{\left[T_{CMB} - T_{ref}\right]}{D}. \tag{20}$$

Because CMB heat flux controls the heat that can be extracted from the core, it has a strong influence on the outer core dynamics and therefore on the properties of the geodynamo. In particular, the total extracted power should not be too low for geodynamo to operate, around 4 TW if the thermal conductivity of the outer core is equal to 20 W m^{-1} K^{-1} (Labrosse 2016), equivalent to a heat flux (on the core side) of about 26 mW m^{-2}. It is interesting to note that, despite the strong uncertainties in the parameters of eq. (20), defining the horizontally averaged CMB heat flux, our estimate of the average lowermost mantle thermal conductivity, $\Lambda_{\mathrm{ref}} = 8.6$ W m^{-1} K^{-1}, together with possible values of the thickness and temperature jump of the thermal boundary layer, $D = 200$ km and $\Delta T_{\mathrm{ref}} = 750$ K, leads to a reference CMB heat flux (on mantle side) of 32 mW m^{-2}. In other words, our modelling is consistent with an efficient powering of the geodynamo.

The amplitude and pattern of CMB heat flux anomalies may influence details of outer core dynamics and alter dynamo actions (e.g. Olson & Christensen 2002; Aubert *et al.* 2007). On mantle side, lateral variations in CMB heat flux are controlled by lateral variations in temperature and thermal conductivity. As temperature increases, the vertical thermal gradient decreases, reducing the CMB heat flux. In addition, thermal conductivity varies locally with temperature and composition (Section 3). Temperature has thus both a direct and an indirect (by changing thermal conductivity) effect on CMB heat flux. Relative variations in CMB heat flux with respect to reference heat flux Φ_{ref} (eq. 20) may be decomposed into variations due to anomalies in the radial temperature jump, ΔT, and anomalies in thermal conductivity, Λ, following

$$\mathrm{dln}\Phi_{\mathrm{CMB}}\ (\varphi,\theta) = \frac{\left[\Delta T\,(\varphi,\theta) - \Delta T_{ref}\right]}{\Delta T_{ref}}\ + \mathrm{dln}\Lambda\,(\varphi,\theta)\,, \tag{21}$$

where $\Delta T(\varphi,\theta) = [T_{\mathrm{CMB}}—T(\varphi,\theta)]$ and $\Delta T_{\mathrm{ref}} = (T_{\mathrm{CMB}}—T_{\mathrm{ref}})$ are the radial temperature jump at local and reference temperature, respectively, and dln$\Lambda(\varphi,\theta)$ is the relative variation in thermal conductivity at longitude φ and latitude θ. A more practical expression of dlnΦ_{CMB} can be obtained by decomposing dlnΛ into its thermal, dlnΛ^{T}, and compositional contributions, and by noting that ΔT can be split as

$$\Delta T\ (\varphi,\theta) = \ \Delta T_{ref} - \mathrm{d}T\,(\varphi,\theta)\,, \tag{22}$$

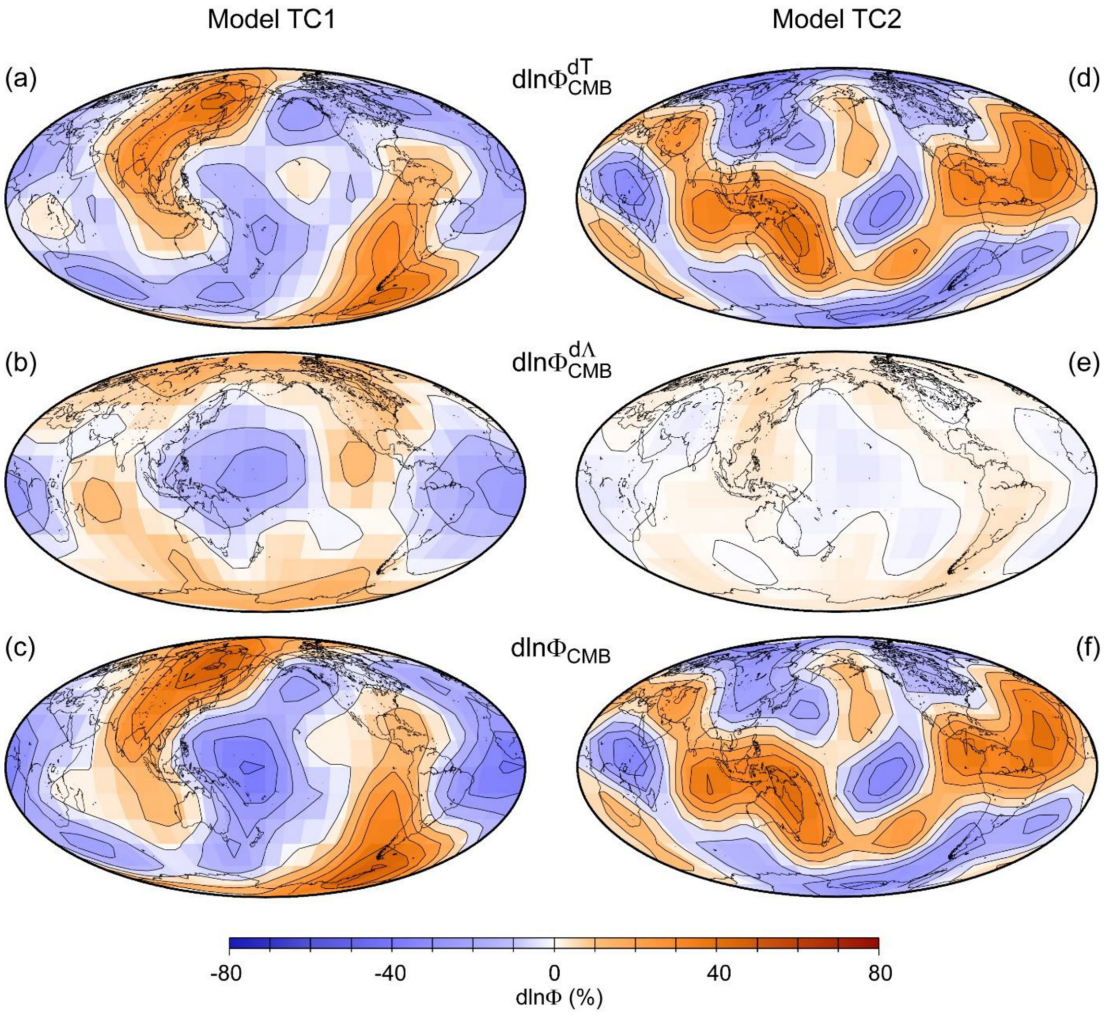

Figure 11. Relative variations in core–mantle boundary (CMB) heat flux inferred from thermochemical models TC1 (left-hand column) and TC2 (right-hand column). First and second rows plot relative anomalies due to explicit variations in temperature (first term of the right-hand-side of eq. 23) and to variations in thermal conductivity (second, third and fourth terms of the right-hand-side of eq. 23), respectively. The last row show the total variation (eq. 23). The reference temperature and temperature jump are $T_r = 3000$ K and $\Delta T_{ref} = 750$ K, respectively. The reference composition is $X_{Bm,ref} = 0.8$ and $X_{Fe,ref} = 0.09$, and the iron partitioning $K_D = 0.4$. Aggregate thermal conductivity is estimated from the geometric average of Hashin–Shtrikman bounds. Horizontal parametrization are the same as in Fig. 9. Contour levels are 10 per cent on all plots.

where $dT(\varphi,\theta) = [T(\varphi,\theta)—T_{ref}]$ is the lateral variation in temperature with respect to T_{ref} at location (φ,θ). Relative variations in heat flux can then be written

$$d\ln\Phi_{CMB}\ (\varphi,\theta) = -\frac{dT\,(\varphi,\theta)}{\Delta T_{ref}} + d\ln\Lambda^{T} + d\ln\Lambda^{Bm} + d\ln\Lambda^{Fe}. \tag{23}$$

The first term in the right-hand-side of eq. (23), $-dT/\Delta T_{ref}$, quantifies the heat flux anomalies directly related to temperature anomalies, while the three other terms describe the heat flux anomalies due to changes in thermal conductivity (section 3.5). eq. (23) further requires the knowledge of the CMB temperature (T_{CMB}), and of the reference mantle geotherm (T_{ref}), which are both not well constrained. These values, or equivalently the value of ΔT_{ref}, are controlling the relative influence of the thermal and compositional contributions to heat flux anomalies.

Fig. 11 shows maps of CMB heat flux anomalies, $d\ln\Phi_{CMB}$, inferred from models TC1 and TC2 following eq. (23) and for $\Delta T_{ref} = 750$ K. For both models, $d\ln\Phi_{CMB}$ are clearly dominated by lateral temperature anomalies [first term in the right-hand-side of eq. (23), $d\ln\Phi^{dT}_{CMB} = -dT/\Delta T_{ref}$]. Variations in thermal conductivity triggered by thermal and compositional changes, given by the sum $d\ln\Phi^{d\Lambda}_{CMB} = d\ln\Lambda^{T} + d\ln\Lambda^{Bm} + d\ln\Lambda^{Fe}$, only have a small to moderate influence on $d\ln\Phi_{CMB}$. For model TC1, the rms in $d\ln\Phi^{dT}_{CMB}$ and $d\ln\Phi^{d\Lambda}_{CMB}$ are equal to 17.6 and 9.9 per cent, respectively (Table 2). In model model TC2 heat flux anomalies related to thermal conductivity changes are even smaller, with rms in $d\ln\Phi^{d\Lambda}_{CMB}$ of only 2.6 per cent (compared to 20.4 per cent for $d\ln\Phi^{dT}_{CMB}$; Table 2). Amplitude in $d\ln\Phi_{CMB}$ reaches ±40 per cent for model TC2, and slightly more for model TC1. eq. (23) indicates that this amplitude depends on ΔT_{ref}. More specifically, increasing ΔT_{ref} reduces $d\ln\Phi^{dT}_{CMB}$ but leaves $d\ln\Phi^{d\Lambda}_{CMB}$ unchanged. As a result, the amplitude of heat flux anomalies decrease with increasing ΔT_{ref} (Fig. 12a) and the relative contribution of $d\ln\Phi^{d\Lambda}_{CMB}$ to $d\ln\Phi_{CMB}$ gets stronger. Due to structural differences in the

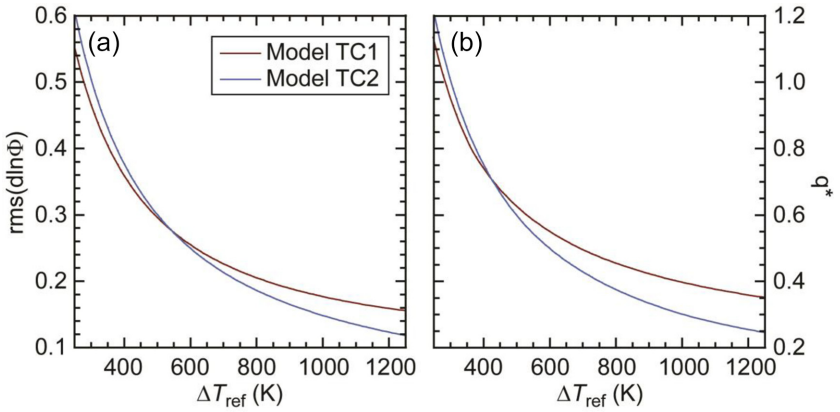

Figure 12. (a) Root mean square in relative anomalies of CMB heat flux, and (b) level of CMB heat flux heterogeneity, measured with $q*$, as a function of the reference temperature jump, $\Delta T_{\rm ref}$, and for two thermochemical models of lowermost mantle, models TC1 and TC2 (Fig. 9). The reference temperature is $T_{\rm r} = 3000$ K, the reference composition $X_{\rm Bm,ref} = 0.8$ and $X_{\rm Fe,ref} = 0.09$, and the iron partitioning $K_{\rm D} = 0.4$. Aggregate thermal conductivity is estimated from the geometric average of Hashin–Shtrikman bounds.

thermal, and to a lesser extent compositional, distributions of models TC1 and TC2, heat flux patterns inferred from models TC1 and TC2 are substantially different. Both models are dominated by spherical harmonic degree $l = 2$ anomalies, and contain smaller scale anomalies. Smaller scale anomalies are, however, more pronounced in model TC2 than in model TC1. As a result, high heat flux regions are located beneath Japan, Katchamka and the southern tip of South America in model TC1, and beneath Indonesia, Australia and mid-Atlantic in model TC2. It is further interesting to note that, like the variations in thermal conductivity, the lateral variations in CMB heat flux are only slightly affected by the temperature-dependence of thermal conductivity (exponent n in eq. (2)). As n decreases from 1.0 to 0.2, and in the case of model TC1, the rms in $\mathrm{dln}\Phi_{\rm CMB}$ is reduced by 0.03, from 0.235 to 0.203 (Table 3).

To date, there is no consensus on the level of heat flux heterogeneity required to substantially affect geodynamo. The level of heat flux heterogeneity is usually measured with the q^* parameter,

$$q^* = \frac{(\Phi_{max} - \Phi_{min})}{2\Phi_{ref}}\,, \tag{24}$$

where $\Phi_{\rm max}$ and $\Phi_{\rm min}$ are the maximum and minimum in CMB heat flux, and $\Phi_{\rm ref}$ is its horizontally average. Olson & Christensen (2002) noted that dynamo actions are lost if $q^* > 1$, but more recent studies reported successful dynamos with $q^* > 1$ (Dietrich & Wicht 2013). At lower values of q^*, CMB heat flux heterogeneities may still influence the outer core flow. For instance, Aubert *et al.* (2007) pointed out that even modest CMB heat flux heterogeneities, with q^* around 0.2, could influence this flow in such a way that it would induce observable signatures in geomagnetic data. In our modelling, q^* slightly depends on the exponent n controlling the effect of temperature on thermal conductivity (Table 3), and decreases more strongly with increasing $\Delta T_{\rm ref}$, from about 1.1 at $\Delta T_{\rm ref} = 250$ K, to 0.4 and 0.3 (for models TC1 and TC2, respectively) at $\Delta T_{\rm ref} = 1000$ K (Fig. 12b). For $\Delta T_{\rm ref} = 750$ K, it is equal to 0.47 and 0.40 for models TC1 and TC2, respectively. Values of q^* are larger than 1 only if $\Delta T_{\rm ref} < 300$ K, and remains larger than 0.2 for the range of $\Delta T_{\rm ref}$ we explored. Therefore, if real CMB heat flux resembles that predicted by models TC1 and TC2, outer core flow may experience significant mantle control through heat flux variations on mantle side. It is worth noting that neglecting compositional anomalies would require much larger temperature anomalies to explain observed seismic tomography (e.g. Deschamps *et al.* 2012), around 2000–3000 K peak-to-peak for shear-velocity anomalies of ±2.5 per cent. This, in turn, implies that q^* much larger than 1. If, as suggested by Olson & Christensen (2002), dynamo effects are lost for $q^* > 1$, the existence of a geodynamo on Earth invalidates a purely thermal lower mantle.

Finally, details of the heat flux distribution may also influence the outer core flow and the geodynamo. A key observation that is often used for comparison is the geomagnetic flux at the CMB (Jackson *et al.* 2000). High heat flux regions focus magnetic field lines and lead to local highs in the CMB geomagnetic flux. Gubbins *et al.* (2007) suggested that spherical harmonic degree and order $l = 2$ and $m = 2$ (Y_2^2) heat flux patterns recover the observed geomagnetic flux at CMB well, and that this pattern may be imposed by lower mantle heterogeneities, More precisely, lower mantle heterogeneities may control the longitudinal distribution of the intense flux patches observed at high latitude (the latitude of these patches being constrained by the inner core tangent cylinder). Geomagnetic flux patches are also observed at low latitudes, but their existence is less well understood, in particular because the outer core equatorial upwelling predicted by numerical dynamos disperse magnetic field lines at low latitudes (Amit & Olson 2006). It has been suggested that the location of low latitude patches may be controlled by small scale ($l > 2$) thermochemical heterogeneities at the bottom of the mantle (Amit & Choblet 2012). In particular, Amit *et al.* (2017) run numerical simulations of geodynamo in which they imposed distributions of CMB heat flux derived from the thermochemical model of Mosca *et al.* (2012), and found that these simulations reproduce the latitudinal distribution of geomagnetic flux patches better than simulations using heat flux maps built from purely thermal Y_2^2 patterns. Heat flux patterns inferred from models TC1 and TC2 are both dominated by spherical harmonic $l = 2$, but also contain smaller scale complexities that differ for each model (Fig. 11). Heat flux inferred from model TC2 is very

similar to that used by Amit *et al.* (2017), the main difference being that it takes into account heat flux variations related to changes in thermal conductivity. Numerical simulations of geodynamo using this heat flux map as boundary condition may thus be very similar to those obtained by Amit *et al.* (2017), and should thus include low latitude patches. In the heat flux map derived from model TC1, by contrast, the Y_2^2 term is more pronounced, and geodynamo simulations using this pattern as boundary condition may have no or few low latitude patches. Assessing the detailed influence of heat flux patterns inferred from models TC1 and TC2 on CMB geomagnetic flux, however, requires running specific simulations for each of these two models.

6 CONCLUDING DISCUSSION

Using a self-consistent mineral physics data set for thermal conductivities of lower mantle minerals at high pressure, we quantified variations in mantle thermal conductivity induced by changes in temperature and iron and bridgmanite fractions at lowermost mantle conditions. An interesting result is that LLSVPs, if hotter than average mantle and enriched in iron and bridgmanite, should be less thermally conductive than the surrounding mantle, which may in turn alter the dynamics of these structures. By contrast, compared to the direct effect of temperature variations, thermal conductivity anomalies have only a limited impact on lateral variations in CMB heat flux and may not substantially alter outer core dynamics. Saturation and threshold effects, if occurring, are likely to decrease the aggregate conductivity and its relative anomalies. However, quantifying these effects requires new measurements of the thermal conductivities of bridgmanite with iron fraction around 0.05 or less, and ferropericlase with iron fraction in the range 0.15–0.40.

Our modelling is based on lattice thermal conductivities of lower mantle minerals. Lattice thermal conductivity controls heat transfer through lattice vibrations (i.e. phonons), and is usually considered to be the dominant contribution to the thermal conductivity of Earth's mantle. Heat transfer may also be operated by migrations of electrons (electronic conductivity) or photons (radiative heat transfer), the total (effective) thermal conductivity being the sum of lattice, electronic, and radiative conductivities. Electronic conductivity is important in metals, but is negligible in mantle minerals. By contrast, the contribution of radiative heat transfer is still a matter of debate (Hofmeister & Yuen 2007; Goncharov *et al.* 2006; Keppler *et al.* 2008; Kavner & Rainey 2016). Radiative conductivity of lower mantle minerals is strongly reduced by the presence of iron, and is left mostly unaffected by iron spin transitions (Goncharov *et al.* 2010). Effects of temperature and pressure on radiative conductivity are opposite to those on lattice thermal conductivity, *i.e.* radiative conductivity increases with temperature but deceases with increasing pressure, due to larger optical absorption. Therefore, heat transfer may be influenced by radiative transport at high temperatures, but in the lowermost mantle this contribution might be compensated or attenuated by high pressure. For instance, it is interesting to note that, along a geotherm, the increase in pressure compensates the effect due to adiabatic temperature increase with depth (Kavner & Rainey 2016). Experimentally, radiative conductivity is estimated from optical properties of mineral, but differences in methods and mineral structures lead to large discrepancies in the estimated values of the radiative conductivity. Yet, available data overall indicate that at lower mantle conditions, radiative conductivity remains much smaller than lattice thermal conductivity. Keppler *et al.* (2008) found that the radiative conductivity of bridgmanite with $x_{Fe}^{Bm} = 0.1$ at $T_r = 3000$ K and 125 GPa is about 3.0 W m^{-1} K^{-1}. Hofmeister and Yuen (2007) calculated mantle radiative conductivity along possible mantle geotherms, and found 2.0 W m^{-1} K^{-1} for an aggregate with 12 per cent iron. Based on optical absorption spectra for bridgmanite ($x_{Fe}^{Bm} = 0.1$) and ferropriclase ($x_{Fe}^{Fp} = 0.15$) samples, Goncharov *et al.* (2005), obtained even lower values, around 0.5 W m^{-1} K^{-1}. Kavner & Rainey (2016) developed a consistent approach that incorporates data sets from Keppler *et al.* (2008) and Goncharov *et al.* (2008), and used this approach to estimate an upper bound for radiative conductivity. For an aggregate with $X_{Bm} = 0.8$, this upper estimate is in the range 0.7–5.0 W m^{-1} K^{-1} throughout the lower mantle. In comparison, the lattice conductivity for a pyrolitic mantle ($X_{Bm} = 0.8$ and $X_{Fe} = 0.09$) at $T_r = 3000$ K and 134 GPa deduced from the measurements of Hsieh *et al.* (2017, 2018) is around 8.6 W m^{-1} K^{-1}. Clearly, describing heat transfer in Earth's lower mantle with only lattice thermal conductivity is a good approximation.

More importantly, lowermost mantle thermal conductivity may be affected by structural and compositional changes that are not accounted for in our models, in particular the presence at the bottom of the mantle of post-perovskite (pPv) and of recycled oceanic crust (MORB). Because pPv is not stable at high temperature, it may not be present within LLSVPs. The presence of pPv outside LLSVPs is accounted for in models TC2, resulting in a strong decrease in the amplitude of anomalies in bridgmanite and in the variations in thermal conductivity. However, in absence of experimental constraints on the thermal conductivity of this mineral, the direct impact of pPv on mantle conductivity cannot be assessed. If, for instance, pPv is more conductive than bridgmanite, relative anomalies in thermal conductivity would increase in amplitude compared to the anomalies mapped in Fig. 10(h). Subducted oceanic crust may reach the bottom of the mantle (van der Hilst *et al*. 1997) and accumulate there, in which case they may contribute to observed seismic anomalies. Numerical simulations indicate that small amounts of recycled MORB may be incorporated in LLSVPs (Tackley 2012; Li *et al.* 2014). LLSVPs are, however, unlikely composed only of recycled MORB, as it would require exaggerated temperature excess, around 1500 K, to explain observed seismic anomalies (Deschamps *et al.* 2012). Because MORB are enriched in iron and free of ferropericlase, one would expect the thermal conductivity of MORB to be lower than that of surrounding mantle. However, MORB may also be colder than average, which would balance a potential intrinsic (chemical) reduction of conductivity. Again, in absence of constraints on the thermal conductivity of MORB at high pressure, it is not possible to estimate their impact on lower mantle thermal conductivity. Finally, ULVZs, if hotter than average mantle and strongly enriched in iron (Mao *et al.* 2006; Wicks *et al.* 2010), may locally affect thermal conductivity and CMB heat flux. Hsieh *et al.* (2018) estimated that thermal conductivity within these regions may be reduced down to about 2 W m^{-1} K^{-1} if ULVZs are enriched in iron by 20

per cent. While such low conductivities may impact the evolution of ULVZs, their influence on the lower mantle and outer core dynamics may be limited, as ULVZs are small and local structures, typically a few hundreds of kilometres across (for a recent review, see Yu & Garnero 2018).

Despite these limitations, our mapping of lowermost mantle thermal conductivity indicates that this parameter may substantially vary in the deep mantle, possibly influencing lower mantle dynamics. Additional experimental studies for lower mantle minerals, including post-perovskite, together with numerical simulations of thermochemical convection accounting for lateral variations in conductivity will help refining lowermost mantle thermal conductivity maps and assessing the influence of these variations on mantle dynamics.

ACKNOWLEDGEMENTS

We are grateful to two anonymous colleagues for their reviews, and to Dylan Meier for his editing and suggestions. This research was funded by Academia Sinica grants AS-102-CDA-M02 (FD) and AS-106-CDA-M02 (WH), and by the Ministry of Science and Technology (MoST) of Taiwan grants 106–2116-M-001–014 (FD) and 105–2116-M-001–024 and 106–2116-M-001–022 (WH).

REFERENCES

Amit, H. & Choblet, G., 2012. Mantle-driven geodynamo features–effects of compositional and narrow D" anomalies, *Phys. Earth planet. Inter.,* **190–191,** 34–43.

Amit, H., Deschamps, F. & Choblet, G., 2017. Numerical dynamos with outer boundary heat flux inferred from probabilistic tomography - consequences for latitudinal distribution of magnetic flux, *Geophys. J. Int.,* **203,** 840–855.

Amit, H. & Olson, P., 2006. Time-average and time-dependent parts of core flow, *Phys. Earth planet. Inter.,* **155,** 120–139.

Aubert, J., Amit, H. & Hulot, G., 2007. Detecting thermal boundary control in surface flows from numerical dynamos, *Phys. Earth planet. Inter.,* **160,** 143–156.

Badro, J., 2014. Spin transitions in mantle minerals, *Annu. Rev. Earth planet. Sci.,* **42,** 231–248.

Chang, Y.-Y., Hsieh, W.-P., Tan, E. & Chen, J., 2017. Hydration reduced lattice thermal conductivity of olivine in Earth's upper mantle, *Proc. Nat. Acad. Sci.,* **114,** 4078–4081.

Dalton, D.A., Hsieh, W.-P., Hohensee, G.T., Cahill, D.G. & Goncharov, A.F., 2013. Effect of mass disorder on the lattice thermal conductivity of MgO periclase under pressure. *Sci. Rep.,* **3,** 2400.

Dekura, H., Tsuchiya, T. & Tsuchiya, J., 2013. *Ab initio* lattice thermal conductivity of $MgSiO_3$ perovskite as found in Earth's lower mantle, *Phys. Rev. Lett.,* **110,** 025904.

Deschamps, F., Cobden, L. & Tackley, P.J., 2012. The primitive nature of large low shear-wave velocity provinces, *Earth planet. Sci. Lett.,* **349–350,** 198–208.

Deschamps, F. & Khan, A., 2016. Electrical conductivity as a constraint on lower mantle thermo-chemical structure, *Earth planet. Sci. Lett.,* **450,** 108–119.

Deschamps, F. & Trampert, J., 2003. Mantle tomography and its relation to temperature and composition, *Phys. Earth planet. Inter.,* **140,** 277–291.

Dietrich, W. & Wicht, J., 2013. A hemispherical dynamo model: implications for the Martian crustal magnetization, *Phys. Earth planet. Inter.,* **217,** 10–21.

Dubuffet, F. & Yuen, D.A., 2000. A thick pipe-like heat-transfer mechanism in the mantle: nonlinear coupling between 3-D convection and variable thermal conductivity, *Geophys. Res. Lett.,* **27,** 17–20.

Dubuffet, F., Yuen, D.A. & Yanagawa, T., 2000. Feedback effects of variable thermal conductivity on the cold downwellings in high Rayleigh number convection, *Geophys. Res. Lett.,* **27,** 2981–2984.

Dziewonski, A.M. & Anderson, D.L., 1981. Preliminary reference Earth model, *Phys. Earth planet. Inter.,* **25,** 297–356.

Goncharov, A.F., Haugen, B.D., Beck, P., Struzhkin, V.V. & Jacobsen, S.D., 2006. Radiative conductivity in Earth's lower mantle, *Nature,* **456,** 231–234.

Goncharov, A.F. *et al.*, 2010. Effect of composition, structure, and spin state on the thermal conductivity of the Earth's lower mantle, *Phys. Earth planet. Inter.,* **180,** 148–163.

Goncharov, A.F. *et al.* 2015. Experimental study of thermal conductivity at high pressures: implications for the deep Earth's interior, *Phys. Earth planet. Inter.,* **247,** 11–16.

Gubbins, D., Willis, A.P. & Sreenivasan, B., 2007. Correlation of Earth's magnetic field with lower mantle thermal and seismic structure, *Phys. Earth planet. Inter.,* **162,** 256–260.

Hashin, Z. & Shtrikman, S., 1962. A variational approach to the theory of the effective magnetic permeability of multiphase materials, *J. appl. Phys.,* **33,** 3125–3131.

Hernlund, J. & Houser, C., 2008. On the statistical distribution of seismic velocities in Earth's deep mantle, *Earth planet. Sci. Lett.,* **265,** 423–437.

Hill, R., 1963. Elastic properties of reinforced solids: some theoretical principles, *J. Mech. Phys. Solids,* **11,** 357–372.

Hofmeister, A.M., 1999. Mantle values of thermal conductivity and the geotherm from phonon lifetimes, *Science,* **283,** 1699–1706

Hofmeister, A.M. & Yuen, D.A., 2007. Critical phenomena in thermal conductivity: implications for lower mantle dynamics, *J. Geodyn,* **44,** 186–199.

Hsieh, W.-P., Deschamps, F., Okuchi, T. & Lin, J.F., 2017. Reduced lattice thermal conductivity of Fe-bearing bridgmanite in Earth's deep mantle, *J. geophys. Res.: Solid Earth,* **122,** 4900–4917.

Hsieh, W.-P., Deschamps, F., Okuchi, T. & Lin, J.F., 2018. Effects of iron on the lattice thermal conductivity and dynamics of Earth's deep mantle, *Proc. Nat. Acad. Sci.,* **115,** 4099–4104.

Irifune, T., Shinmei, T., McCammon, C.A., Miyajima, N., Rubie, D.C. & Frost, D.J., 2010. Iron partitioning and density changes of pyrolite in Earth's lower mantle, *Science,* **327,** 193–195.

Ishii, M. & Tromp, J., 1999. Normal-mode and free-air gravity constraints on lateral variations in velocity and density of Earth's mantle, *Science,* **285,** 1231–1236.

Jackson, A., Jonkers, A.R.T. & Walker, M.R., 2000. Four centuries of geomagnetic secular variation from historical records, *Phil. Trans. R. Soc. Lond., A,* **358,** 957–990.

Kavner, A. & Rainey, E.S.G., 2016. Heat transfer in the core and mantle, in *Deep Earth: Physics and Chemistry of the Lower Mantle and Core, 217,* , pp. 31−42, *Geophysical Monograph*, eds Teresaki, H. & Fischer, R.A., American Geophysical Union.

Keppler, H., Dubrovinsky, L.S., Narygina, O. & Kantor, I., 2008. Optical absorption and radiative thermal conductivity of silicate perovskite to 125 GPa, *Science,* **322,** 1529–1532.

Khan, A. & Shankland, T.J., 2012. A geophysical perspective on mantle water content and melting: Inverting electromagnetic sounding data using laboratory-based electrical conductivity profiles, *Earth planet. Sci. Lett.,* **317–318,** 27–43.

Klemens, P.G., White, G.K. & Tainsh, R.J., 1962. Scattering of lattice waves by point defects, *Philos. Mag.,* **7,** 1323–1335.

Labrosse, S., 2016. Thermal state and evolution of the Earth core and deep mantle, in *Deep Earth: Physics and Chemistry of the Lower Mantle and Core, Geophysical Monograph Ser*. 217, 43–54, eds Terasaki, H. & Fischer, R.A., American Geophysical Union.

Lau, H.C.P., Mitrovica, J.X., Davis, J.L., Tromp, J., Yang, H.-Y. & Al-Attar, D., 2017. Tidal tomography constraints Earth's deep mantle buoyancy, *Nature,* **551,** 321–326.

Li, M., McNamara, A.K. & Garnero, E.J., 2014. Chemical complexity of hotspots caused by cycling oceanic crust through mantle reservoirs, *Nature Geoscience,* **7,** 366–370

Li, M. & Zhong, S., 2017. The source location of mantle plumes from 3D spherical models of mantle convection, *Earth planet. Sci. Lett.,* **478,** 47–57.

Manthilake, G.M., de Koker, N., Frost, D.J. & McCammon, C., 2011. Lattice thermal conductivity of lower mantle minerals and heat flux from Earth's core, *Proc. Nat. Acad. Sci.,* **114,** 4078–4081.

Mao, W.L. *et al.*, 2006. Iron-rich post-perovskite and the origin of ultralow-velocity zones, *Science,* **312,** 564–566.

Masters, G., Laske, G., Bolton, H. & Dziewonski, A.M., 2000. The relative behavior of shear velocity, bulk sound speed, and compressional velocity in the mantle: implicationfor thermal and chemical structure, eds Karato, S.-I. et al., in *Earth's Deep Interior: Mineral Physics and Tomography from the Atomic to the Global Scale, Geophysical Monograph. 117,* American Geophysical Union, pp. 63–87.

Mosca, I., Cobden, L., Deuss, A., Ritsema, J. & Trampert, J., 2012. Seismic and mineralogical structures of the lower mantle from probabilistic tomography, *J. geophys. Res.: Solid Earth,* **117**.

Ohta, K., Yagi, T., Hirose, K. & Ohishi, Y., 2017. Thermal conductivity of ferropericlase in the Earth's lower mantle, *Earth planet. Sci. Lett.,* **465,** 29–37.

Ohta, K., Yagi, T., Taketoshi, N., Hirose, K., Komabayashi, T., Baba, T., Ohishi, Y. & Hernlund, J., 2012. Lattice thermal conductivity of $MgSiO_3$ perovskite and post-perovskite at the core–mantle boundary, *Earth planet. Sci. Lett.,* **349–350,** 109–115.

Olson, P. & Christensen, U.R., 2002. The time-averaged magnetic field in numerical dynamos with non-uniform boundary heat flow, *Geophys. J. Int.,* **151,** 809–823.

Piet, H., Badro, J., Nabiei, F., Dennenwaldt, T., Shim, S.-H., Cantoni, M., Hébert, C. & Gillet, P., 2016. Spin and valence dependence of iron partitioning in Earth's deep mantle, *Proc. Nat. Acad. Sci.,* **113,** 1127–11130.

Ritsema, J., Deuss, A., vanHeijst, H.-J. & Woodhouse, J.H., 2011. S40RTS: a degree-40 shear-velocity model for the mantle from new Rayleigh wave dispersion, teleseismic traveltime and normal-mode splitting function measurements, *Geophys. J. Int.,* **184,** 1223–1236.

Stackhouse, S., Stixrude, L. & Karki, B.B., 2015. First-principles calculations of the lattice thermal conductivity of the lower mantle, *Earth planet. Sci. Lett.,* **427,** 11–17.

Tackley, P.J., 1998. Three-dimensional simulations of mantle convection with a thermo-chemical CMB boundary layer: D"?, in *The Core-mantle Boundary Region, Geodyn. Ser., 28,* pp. 231–253, eds Gurnis, M. *et al.*, American Geophysical Union.

Tackley, P.J., 2012), Dynamics and evolution of the deep mantle resulting from thermal, chemical, phase and melting effects, *Earth-Sci. Rev.*, **110,** 1–25.

Trampert, J., Deschamps, F., Resovsky, J.S. & Yuen, D.A., 2004. Probabilistic tomography maps significant chemical heterogeneities in the lower mantle, *Science,* **306,** 853–856.

Trampert, J., Vacher, P. & Vlaar, N., 2001. Sensitivities of seismic velocities to temperature, pressure and composition in the lower mantle, *Phys. Earth planet. Inter.,* **124,** 255–267.

van der Hilst, R.D. & Kárason, H., 1999. Compositional heterogeneity in the bottom 1000 kilometers of Earth's mantle: towards a hybrid convection model, *Science,* **283,** 1885–1888.

van der Hilst, R.D., Widiyantoro, S. & Engdahl, E.R., 1997. Evidence for deep mantle circulation from seismic tomography, *Nature,* **386,** 578–584.

Wicks, J.K., Jackson, J.M. & Sturhahn, W., 2010. Very low sound velocities in iron-rich, Mg,Fe)O: Implications for the core-mantle boundary region, *Geophys. Res. Lett.,* **37,** L15304.

Xu, Y., Shankland, T.J., Linhardt, S., Rubie, D.C., Langenhorst, F. & Klasinski, K., 2004. Thermal diffusivity and conductivity of olivine, wadsleyite and ringwoodite to 20 GPa and 1373 K, *Phys. Earth planet. Inter.,* **143,** 321–336.

Yu, S. & Garnero, E.J., 2018. Ultralow velocity zone locations: a global assessment, *Geochem. Geophys. Geosys.,* **19,** 396–414.

APPENDIX

The individual fractions of iron in bridgmanite and ferropericlase, x_{Fe}^{Bm} and x_{Fe}^{Fp}, can be obtained by solving eqs (3) and (4), which give the global fraction iron, $X_{\rm Fe}$, and iron partitioning, $K_{\rm D}$, respectively, as a function of the volume fraction of bridgmanite in the aggregate, $X_{\rm Bm}$, and of x_{Fe}^{Bm} and x_{Fe}^{Fp}. Combining these equations, one gets two 2nd order polynomials, one in x_{Fe}^{Bm} and one in x_{Fe}^{Fp}. Each of these two polynomials has only one positive solution, which gives the expression of x_{Fe}^{Bm} and x_{Fe}^{Fp}:

$$x_{Fe}^{Bm} = \frac{1 + (X_{Bm} + X_{Fe})(K_D - 1) - \sqrt{[1 + (X_{Bm} + X_{Fe})(K_D - 1)]^2 - 4X_{Bm}(K_D - 1)K_D X_{Fe}}}{2X_{Bm}(K_D - 1)} \tag{A1}$$

and

$$x_{Fe}^{Fp} = -\frac{1 + (X_{Bm} - X_{Fe})(K_D - 1) - \sqrt{[1 + (X_{Bm} - X_{Fe})(K_D - 1)]^2 + 4(1 - X_{Bm})(K_D - 1)X_{Fe}}}{2(1 - X_{Bm})(K_D - 1)}. \tag{A2}$$

The thermal conductivity of an aggregate of bridgmanite and ferropericlase depends on both the global fraction in iron of the aggregate, $X_{\rm Fe}$, and its volume fraction of bridgmanite, $X_{\rm Bm}$. If the aggregate conductivity is defined by the geometric average of the lower and upper HS bounds, $\Lambda_{\rm HS-}$ and $\Lambda_{\rm HS+}$, relative anomalies in the aggregate conductivity are given by

$$\mathrm{d}\ln \Lambda_{HSm}^{Bm} = \frac{1}{\Lambda_{ref}} \frac{\partial \Lambda_{HSm}}{\partial X_{Bm}} \mathrm{d}X_{Bm} = \frac{1}{2\Lambda_{ref}} \left(\sqrt{\frac{\Lambda_{HS+}}{\Lambda_{HS-}}} \frac{\partial \Lambda_{HS-}}{\partial X_{Bm}} + \sqrt{\frac{\Lambda_{HS-}}{\Lambda_{HS+}}} \frac{\partial \Lambda_{HS+}}{\partial X_{Bm}} \right) \mathrm{d}X_{Bm}, \tag{A3}$$

and

$$\mathrm{d}\ln \Lambda_{HSm}^{Fe} = \frac{1}{\Lambda_{ref}} \frac{\partial \Lambda_{HSm}}{\partial X_{Fe}} \mathrm{d}X_{Fe} = \frac{1}{2\Lambda_{ref}} \left(\sqrt{\frac{\Lambda_{HS+}}{\Lambda_{HS-}}} \frac{\partial \Lambda_{HS-}}{\partial X_{Fe}} + \sqrt{\frac{\Lambda_{HS-}}{\Lambda_{HS+}}} \frac{\partial \Lambda_{HS+}}{\partial X_{Fe}} \right) \mathrm{d}X_{Fe}, \tag{A4}$$

where Λ_{ref} is the conductivity at reference composition $X_{\mathrm{Bm,ref}}$ and $X_{\mathrm{Fe,ref}}$. Partial derivatives of $\Lambda_{\mathrm{HS-}}$ and $\Lambda_{\mathrm{HS+}}$ with respect to X_{Bm} and X_{Fe} can be written

$$\frac{\partial \Lambda_{HS-}}{\partial X_{Bm}} = -\frac{1}{3}\frac{\Lambda_{Bm}\left(\Lambda_{Fp}-\Lambda_{Bm}\right)\left(\Lambda_{Fp}+2\Lambda_{Bm}\right)}{\left[\Lambda_{Bm}+X_{Bm}\left(\Lambda_{Fp}-\Lambda_{Bm}\right)/3\right]^2}+\frac{\partial \Lambda_{HS-}}{\partial \Lambda_{Bm}}\frac{\partial \Lambda_{Bm}}{\partial X_{Bm}}+\frac{\partial \Lambda_{HS-}}{\partial \Lambda_{Fp}}\frac{\partial \Lambda_{Fp}}{\partial X_{Bm}}, \tag{A5}$$

$$\frac{\partial \Lambda_{HS+}}{\partial X_{Bm}} = -\frac{1}{3}\frac{\Lambda_{Fp}\left(\Lambda_{Fp}-\Lambda_{Bm}\right)\left(2\Lambda_{Fp}+\Lambda_{Bm}\right)}{\left[\Lambda_{Fp}-(1-X_{Bm})\left(\Lambda_{Fp}-\Lambda_{Bm}\right)/3\right]^2}+\frac{\partial \Lambda_{HS+}}{\partial \Lambda_{Bm}}\frac{\partial \Lambda_{Bm}}{\partial X_{Bm}}+\frac{\partial \Lambda_{HS+}}{\partial \Lambda_{Fp}}\frac{\partial \Lambda_{Fp}}{\partial X_{Bm}}, \tag{A6}$$

$$\frac{\partial \Lambda_{HS-}}{\partial X_{Fe}} = \frac{\partial \Lambda_{HS-}}{\partial \Lambda_{Bm}}\frac{\partial \Lambda_{Bm}}{\partial X_{Fe}}+\frac{\partial \Lambda_{HS-}}{\partial \Lambda_{Fp}}\frac{\partial \Lambda_{Fp}}{\partial X_{Fe}}, \tag{A7}$$

and

$$\frac{\partial \Lambda_{HS+}}{\partial X_{Fe}} = \frac{\partial \Lambda_{HS+}}{\partial \Lambda_{Bm}}\frac{\partial \Lambda_{Bm}}{\partial X_{Fe}}+\frac{\partial \Lambda_{HS+}}{\partial \Lambda_{Fp}}\frac{\partial \Lambda_{Fp}}{\partial X_{Fe}}. \tag{A8}$$

Eqs (A5)–(A8) involve partial derivatives of HS bounds with respect to the individual conductivities of bridgmanite and ferropericlase, Λ_{Bm} and Λ_{Fp}, which are given by

$$\frac{\partial \Lambda_{HS-}}{\partial \Lambda_{Bm}} = 1-\frac{(1-X_{Bm})\left[\Lambda_{Bm}^2-X_{Bm}\left(\Lambda_{Fp}-\Lambda_{Bm}\right)^2/3\right]}{\left[\Lambda_{Bm}+X_{Bm}\left(\Lambda_{Fp}-\Lambda_{Bm}\right)/3\right]^2}, \tag{A9}$$

$$\frac{\partial \Lambda_{HS-}}{\partial \Lambda_{Fp}} = \frac{(1-X_{Bm})\,\Lambda_{Bm}^2}{\left[\Lambda_{Bm}+X_{Bm}\left(\Lambda_{Fp}-\Lambda_{Bm}\right)/3\right]^2}, \tag{A10}$$

$$\frac{\partial \Lambda_{HS+}}{\partial \Lambda_{Bm}} = \frac{X_{Bm}\,\Lambda_{Fp}^2}{\left[\Lambda_{Fp}-(1-X_{Bm})\left(\Lambda_{Fp}-\Lambda_{Bm}\right)/3\right]^2}, \tag{A11}$$

and

$$\frac{\partial \Lambda_{HS+}}{\partial \Lambda_{Fp}} = 1-\frac{X_{Bm}\left[\Lambda_{Fp}^2-(1-X_{Bm})\left(\Lambda_{Fp}-\Lambda_{Bm}\right)^2/3\right]}{\left[\Lambda_{Fp}-(1-X_{Bm})\left(\Lambda_{Fp}-\Lambda_{Bm}\right)/3\right]^2}. \tag{A12}$$

Derivatives of Λ_{Bm} and Λ_{Fp}, with respect to X_{Fe} and X_{Bm}, which also appear in derivatives of $\Lambda_{\mathrm{HS-}}$ and $\Lambda_{\mathrm{HS+}}$ (eqs A5–A8), may be rewritten as a function of derivatives with respect to individual fractions of iron x_{Fe}^{Bm} and x_{Fe}^{Fp} following:

$$\frac{\partial \Lambda_i}{\partial X_{Bm}} = \frac{\partial \Lambda_i}{\partial x_{Fe}^i}\frac{\partial x_{Fe}^i}{\partial X_{Bm}}, \tag{A13}$$

and

$$\frac{\partial \Lambda_i}{\partial X_{Fe}} = \frac{\partial \Lambda_i}{\partial x_{Fe}^i}\frac{\partial x_{Fe}^i}{\partial X_{Fe}}, \tag{A14}$$

where subscripts and superscripts i stand either for bridgmanite, Bm, or ferropericlase, Fp. Derivatives of x_{Fe}^{Bm} and x_{Fe}^{Fp} with respect to X_{Fe} and X_{Bm} can then be calculated from eqs (A1) and (A2), leading to

$$\frac{\partial \Lambda_{Bm}}{\partial X_{Bm}} = \frac{1}{2X_{Bm}}\left[1-2x_{Fe}^{Bm}-\frac{(1-X_{Bm})+K_D X_{Bm}-X_{Fe}(K_D+1)}{\sqrt{\left[1+(X_{Bm}+X_{Fe})(K_D-1)\right]^2-4X_{Bm}(K_D-1)K_D X_{Fe}}}\right]\frac{\partial \Lambda_{Bm}}{\partial x_{Fe}^{Bm}} \tag{A15}$$

$$\frac{\partial \Lambda_{Fp}}{\partial X_{Bm}} = -\frac{1}{2(1-X_{Bm})}\left[1-2x_{Fe}^{Fp}-\frac{(1-X_{Bm})+K_D X_{Bm}-X_{Fe}(K_D+1)}{\sqrt{\left[1+(X_{Bm}-X_{Fe})(K_D-1)\right]^2+4X_{Fe}(1-X_{Bm})(K_D-1)}}\right]\frac{\partial \Lambda_{Fp}}{\partial x_{Fe}^{Fp}} \tag{A16}$$

$$\frac{\partial \Lambda_{Bm}}{\partial X_{Fe}} = \frac{1}{2X_{Bm}}\left[1-\frac{(1-X_{Bm})-K_D X_{Bm}+X_{Fe}(K_D-1)}{\sqrt{\left[1+(X_{Bm}+X_{Fe})(K_D-1)\right]^2-4X_{Bm}(K_D-1)K_D X_{Fe}}}\right]\frac{\partial \Lambda_{Bm}}{\partial x_{Fe}^{Bm}} \tag{A17}$$

$$\frac{\partial \Lambda_{Fp}}{\partial X_{Fe}} = -\frac{1}{2(1-X_{Bm})}\left[1+\frac{(1-X_{Bm})-K_D X_{Bm}+X_{Fe}(K_D-1)}{\sqrt{\left[1+(X_{Bm}-X_{Fe})(K_D-1)\right]^2+4X_{Fe}(1-X_{Bm})(K_D-1)}}\right]\frac{\partial \Lambda_{Fp}}{\partial x_{Fe}^{Fp}}. \tag{A18}$$

Finally, because we defined conductivity anomalies relatively to a reference conductivity at a reference composition $X_{\mathrm{Bm,ref}}$ and $X_{\mathrm{Fe,ref}}$, the derivatives of Λ_{Bm} with respect to x_{Fe}^{Bm} and Λ_{Fp} with respect to x_{Fe}^{Fp} may be written

$$\frac{\partial \Lambda_{Bm}}{\partial x_{Fe}^{Bm}} = \frac{\left(\Lambda_{Bm} - \Lambda_{Bm,ref}\right)}{\left(x_{Fe}^{Bm} - x_{Fe,ref}^{Bm}\right)} \tag{A19}$$

and

$$\frac{\partial \Lambda_{Fp}}{\partial x_{Fe}^{Fp}} = \frac{\left(\Lambda_{Fp} - \Lambda_{Fp,ref}\right)}{\left(x_{Fe}^{Fp} - x_{Fe,ref}^{Fp}\right)}\,, \tag{A20}$$

where $\Lambda_{\mathrm{Bm,ref}}$ and $\Lambda_{\mathrm{Fp,ref}}$ are the conductivities of bridgmanite and ferroperriclase at reference iron fractions, $x_{Fe,ref}^{Bm}$ and $x_{Fe,ref}^{Fp}$, that is, calculated by solving eqs (3) and (4) with the prescribed $X_{\mathrm{Bm,ref}}$ and $X_{\mathrm{Fe,ref}}$.